JOURNAL OF PETROLOGY | VOLUME 46 | NUMBER 4 | PAGES 749–781 | 2005 | doi:10.1093/petrology/egh096

Phase Relations and Stability of Magnetoplumbite- and Crichtonite-Series Phases under Upper-Mantle *P–T* Conditions: an Experimental Study to 15 GPa with Implications for LILE Metasomatism in the Lithospheric Mantle

JÜRGEN KONZETT[1]*, HEXIONG YANG[2] AND DANIEL J. FROST[3]

[1]INSTITUT FÜR MINERALOGIE UND PETROGRAPHIE, UNIVERSITÄT INNSBRUCK, INNRAIN 52, A-6020 INNSBRUCK, AUSTRIA

[2]DEPARTMENT OF MECHANICAL AND MATERIALS ENGINEERING, FLORIDA INTERNATIONAL UNIVERSITY, 10555 WEST FLAGLER STREET, MIAMI, FL 33175, USA

[3]BAYERISCHES GEOINSTITUT, UNIVERSITÄT BAYREUTH, UNIVERSITÄTSSTRASSE 30, D-95447 BAYREUTH, GERMANY

RECEIVED FEBRUARY 26, 2004; ACCEPTED NOVEMBER 9, 2004
ADVANCE ACCESS PUBLICATION JANUARY 7, 2005

High-pressure–high-temperature experiments were performed in the range 7–15 GPa and 1300–1600°C to investigate the stability and phase relations of the K- and Ba-dominant members of the crichtonite and magnetoplumbite series of phases in simplified bulk compositions in the systems TiO_2–ZrO_2–Cr_2O_3–Fe_2O_3–BaO–K_2O and TiO_2–Cr_2O_3–Fe_2O_3–BaO–K_2O. Both series of phases occur as inclusions in diamond and/or as constituents of metasomatized peridotite mantle xenoliths sampled by kimberlites or alkaline lamprophyres. They can accommodate large ion lithophile elements (LILE) and high field strength elements (HFSE) on a wt % level and, hence, can critically influence the LILE and HFSE budget of a metasomatized peridotite even if present only in trace amounts. The Ba and K end-members of the crichtonite series, lindsleyite and mathiasite, are stable to 11 GPa and 1500–1600°C. Between 11 and 12 GPa, lindsleyite breaks down to form two Ba–Cr-titanates of unknown structure that persist to at least 13 GPa. The high-pressure breakdown product of mathiasite is a K–Cr-titanate with an idealized formula KM_7O_{12}, where M = Ti, Cr, Mg, Fe. This phase possesses space group $P6_3/m$ with a = 9·175(2) Å, c = 2·879(1) Å, V = 209·9(1) Å^3. Towards high temperatures, lindsleyite persists to 1600°C, whereas mathiasite breaks down between 1500 and 1600°C to form a number of complex Ti–Cr-oxides. Ba and K end-members of the magnetoplumbite series, hawthorneite and yimengite, are stable in runs at 7, 10 and 15 GPa between 1300 and 1400°C coexisting with a number of Ti–Cr-oxides. Molar mixtures (1:1) of lindsleyite–mathiasite and hawthorneite–yimengite were studied at 7–10 GPa and 1300–1400°C, and 9–15 GPa and 1150–1400°C, respectively. In the system lindsleyite–mathiasite, one homogeneous Ba–K phase is stable, which shows a systematic increase in the K/(K + Ba) ratio with increasing pressure. In the system hawthorneite–yimengite, two coexisting Ba–K phases appear, which are Ba rich and Ba poor, respectively. The data obtained from this study suggest that Ba- and K-dominant members of the crichtonite and magnetoplumbite series of phases are potentially stable not only throughout the entire subcontinental lithosphere but also under conditions of an average present-day mantle adiabat in the underlying asthenosphere to a depth of up to 450 km. At still higher pressures, both K and Ba may remain stored in alkali titanates that would also be eminently suitable for the transport of other ions with large ionic radii.

KEY WORDS: *crichtonite; magnetoplumbite; high-*P–T *experiments; phase relations; upper mantle*

*Corresponding author. Telephone: +43-(0)512-507-5506. Fax: +43-(0)512-507-2926. E-mail: juergen.konzett@uibk.ac.at

INTRODUCTION

The study of peridotite xenoliths sampled by magmas originating from upper-mantle depths has shown that metasomatism is a widespread phenomenon in the subcontinental mantle lithosphere (e.g. Kempton, 1987; Menzies *et al.*, 1987, and references therein) and is likely to be a prerequisite for the generation of deep-seated incompatible element enriched rocks such as kimberlites, lamproites and alkali basalts (Fraser *et al.*, 1985; Tainton & McKenzie, 1994). More recently, metasomatism involving Ti phases has also been documented in oceanic upper-mantle peridotites sampled by hotspot magmas (Grégoire *et al.*, 2000*a*, 2000*b*). Metasomatism is often characterized by the addition of water and/or incompatible high field strength elements (HFSE) and large ion lithophile elements (LILE), which may lead to the crystallization of both silicate and oxide phases not previously present in the peridotitic upper mantle (see Harte, 1987). The most commonly observed metasomatic silicates are phlogopite and amphibole, which are able to store high concentrations of elements with large ionic radii, such as Ba, Sr, Rb, Cs and Pb, in highly coordinated lattice positions. In many cases, (Fe)Ti-oxides are part of the metasomatic assemblages. The most common metasomatic oxides are rutile and/or ilmenite, which are characteristic of Fe–Ti metasomatism typically found in mantle xenoliths entrained in alkali basalts, but also as part of kimberlitic megacryst suites (e.g. Mitchell, 1977; Menzies *et al.*, 1987; Schulze *et al.*, 1995). Significant amounts of rutile and ilmenite may also be present in metasomatized mantle rocks sampled by kimberlites and lamproites (Dawson & Smith, 1977; Harte *et al.*, 1987) and both phases are present as inclusions in diamond (e.g. Sobolev & Yefimova, 2000, and references therein). In rare cases, armalcolite, which is a member of the pseudobrookite $FeTi_2O_5$–$MgTi_2O_5$ series, may join the metasomatic oxide assemblage in both subcontinental (e.g. Jones *et al.*, 1982; Haggerty, 1983; Jaques *et al.*, 1990; Varlamov *et al.*, 1996) and suboceanic (Grégoire *et al.*, 2000*b*) lithospheric settings. A typical feature of these metasomatic (Fe)Ti-oxides is variable and, in part, extremely high concentrations of Cr and HFSE such as Zr, Hf, Nb and Ta, reaching wt % levels (e.g. Mitchell, 1977; Tollo & Haggerty, 1987; Wang *et al.*, 1999).

A third group of metasomatic oxides that has been reported so far from subcontinental mantle settings only is alkali-bearing titanates of the crichtonite and magnetoplumbite series. These phases are characterized by a layer structure and a highly complex composition (Townes *et al.*, 1967; Grey *et al.*, 1976; Obradors *et al.*, 1985). K–Ba-rich members of both series are present as part of a suite of Ti-oxides involving Cr–Nb-rich rutile, ilmenite, Cr–Ti-spinel and, more rarely, armalcolite $(Fe,Mg)Ti_2O_5$ in xenoliths and/or as xenocrysts sampled by kimberlites or lamprophyres (Jones *et al.*, 1982; Haggerty *et al.*, 1983, 1989; Zhou *et al.*, 1984; Erlank *et al.*, 1987; Nixon & Condliffe, 1989; Kostrovitsky & Garanin, 1991; Varlamov *et al.*, 1996; Kiviets *et al.*, 1998; Wang *et al.*, 1999; Bulanova *et al.*, 2004). The occurrence of Cr–Ti oxides with compositions indicative of crichtonite and magnetoplumbite phases as inclusions in diamond has been reported by Sobolev *et al.* (1988, 1997), Leost *et al.* (2003) and Bulanova *et al.* (2004), and testifies to the high-pressure stability of these phases. Textures of oxide phase intergrowths (Haggerty *et al.*, 1983; Nixon & Condliffe, 1989; Haggerty, 1991; Velde, 2000) indicate that phases of the crichtonite and magnetoplumbite series have formed through metasomatic alteration of pre-existing Ti–Cr oxide-bearing assemblages by LILE–HFSE–rare earth element (REE)-rich fluids or melts in subcontinental lithospheric settings. The very high concentrations of LILE, HFSE and light REE (LREE) (up to 10^3–10^4 times chondritic abundance) in addition to potassium (Haggerty, 1983, 1987; Jones & Ekambaram, 1985; Konzett *et al.*, 2000; Grégoire *et al.*, 2002) found in crichtonite and magnetoplumbite phases, and a pressure stability extending into the stability field of diamond (Foley *et al.*, 1994), make these phases potentially important reservoirs for a large number of incompatible trace elements in the source regions of deep-seated alkaline magmas, such as kimberlites and lamproites (Foley, 1992*a*, 1992*b*; Mitchell, 1995), even if present only in minute amounts. Ti-oxides other than crichtonite and magnetoplumbite series phases that are reported to contain significant amounts of alkali elements include (in very rare cases) armalcolite (see Jaques *et al.*, 1990), priderite $K_2M^{2+}Ti_7O_{16}$–$K_2M^{3+}{}_2Ti_6O_{16}$ (e.g. Mitchell & Lewis, 1983; Mitchell, 1995) and loparite $[(Na,K)_{0.5}REE_{0.5}TiO_3]$–tausonite ($SrTiO_3$)–perovskite ($CaTiO_3$) (LTP) solid solutions. Both priderite and LTP solid solutions have been described as inclusions in diamond (Jaques *et al.*, 1989; Kopylova *et al.*, 1997). It should be noted that apart from their potential as hosts of incompatible (trace) elements in the mantle, phases with crichtonite structure have received attention because of their suitability as storage media for high-level radioactive waste, especially radionuclides with large ionic radii (Krauskopf, 1988).

This study was undertaken to constrain the *P*–*T* stability field of K–Ba-dominant members of the crichtonite and magnetoplumbite series and to identify and characterize their breakdown products. This makes it possible (1) to assess whether crichtonite and magnetoplumbite phases are restricted to the source regions of lithospheric magmas, such as lamproites or alkaline lamprophyres (Fraser *et al.*, 1985; Mitchell & Bergman, 1991; Foley, 1992*a*, 1992*b*) or may be part of deeper asthenospheric enriched sources for group I kimberlites (Mitchell, 1995), and (2) to assess the potential of

these phases as carriers of incompatible trace elements (LILE) as an alternative to, or outside the stability fields of, more common silicate hosts such as micas or amphiboles.

Classification of crichtonite and magnetoplumbite phases

Phases of the crichtonite and magnetoplumbite structural series are characterized by the general formulae $AM_{21}O_{38}$ and $AM_{12}O_{19}$, respectively (Adelsköld, 1938; Rouse & Peacor, 1968). The A- and M-sites are occupied by large and small cations, respectively, and the classification is based on the dominant A-site cation. In the case of the crichtonite series this may be Sr (crichtonite), Ca (loveringite), Na (landauite), U + REE (davidite), Pb (senaite), Ba (lindsleyite), or K (mathiasite) (Haggerty, 1983, and references therein). In the magnetoplumbite series, the Pb-, K-, and Ba-dominant members are magnetoplumbite, yimengite and hawthorneite or haggertyite (Zhou *et al.*, 1984; Grey *et al.*, 1987, 1998; Haggerty *et al.*, 1989). In both series, the M-site may be occupied by Ti, Cr, Fe, Mg, Zr, Nb, V or Zn, with Ti usually accounting for >50% of the M formula position (Haggerty, 1987). The crichtonite structure (rhombohedral *R*-3) is based on a nine-layer close-packed anion lattice in which the A- and M-cations occupy 12-coordinated and 8- or 6-coordinated positions, respectively (Grey *et al.*, 1976; Gatehouse *et al.*, 1983). Magnetoplumbite (hexagonal $P6_3/mmc$) is isostructural with barium ferrite $BaFe_{12}O_{19}$ (Townes *et al.*, 1967; Obradors *et al.*, 1985), and is composed of alternating spinel-like slabs ($M_{12}O_{16}$) with the M-cations in 4- or 6-coordination, and a perovskite-like layer (AMO_3) with the A-cation in 12-fold coordination (Grey *et al.*, 1987).

Natural crichtonite- and magnetoplumbite phases from upper-mantle settings usually show an excess of total cations when normalized to 38 or 19 oxygens, along with a considerable variation in their A- and M-site cation sums (see below), indicating the ability of these structures to accommodate a significant amount of vacancies. Some titanate analyses reported in the literature as crichtonite-group phases combine the high TiO_2 contents (>65 wt %) and very low Cr_2O_3 contents (≤1–2 wt %) typical of pseudobrookite with high concentrations (>1–2 wt %) of LILE and alkali cations such as Ba, Sr, K and Na, the latter typical of crichtonite (e.g. Wang *et al.*, 1999). On the other hand, titanate analyses are reported that show the range in TiO_2 and Cr_2O_3 typical for crichtonite combined with extremely low concentrations of A-site cations (e.g. Varlamov *et al.*, 1996). In the absence of crystal structure data, however, an assignment of phases with these 'hybrid' compositions to a specific group of titanate phases should be made with caution.

EXPERIMENTAL AND ANALYTICAL PROCEDURES

Composition and preparation of starting materials

Six starting compositions were used in the present study, representing simplified end-member compositions of lindsleyite (LI), mathiasite (MA), hawthorneite (HA), yimengite (YI) and 50:50 lindsleyite–mathiasite (LIMA) and hawthorneite–yimengite (HAYI) solid solutions with all Fe as Fe^{3+} ($Fe_{tot} = Fe^{3+}$), following Foley *et al.* (1994). The structural formulae of the starting materials are as follows:

mathiasite $K(Ti_{13}Cr_4FeZrMg_2)O_{38}$;
lindsleyite $Ba(Ti_{12}Cr_4Fe_2ZrMg_2)O_{38}$;
yimengite $K(Ti_3Cr_5Fe_2Mg_2)O_{19}$;
hawthorneite $Ba(Ti_3Cr_4Fe_2Mg_3)O_{19}$;
LIMA $(Ba_{0.5}K_{0.5})(Ti_{13}Cr_{3.5}FeZrMg_{2.5})O_{38}$;
YIHA $(Ba_{0.5}K_{0.5})(Ti_3Cr_{4.5}Fe_2Mg_{2.5})O_{19}$.

The mineral compositions in terms of wt % of the constituent oxides are given in Table 1. In addition, a high-pressure breakdown product of mathiasite with the average composition listed in Table 1 (bulk composition VII) was synthesized for crystallographic study.

Experimental and analytical conditions

The starting materials (Table 1) were synthesized from high-purity (≥99·99%) oxides following the procedure described by Foley *et al.* (1994). Experiments (Table 2) were performed with 600 t and 500 t Walker-type multi-anvil presses at the Geophysical Laboratory (GL) of the Carnegie Institution of Washington and the Bavarian Research Institute of Experimental Geochemistry and Geophysics, University of Bayreuth (BGI), respectively. Assembly sizes and materials are as follows: at the GL: $P \leq 10$ GPa: 18/11 (18 mm edge-length of octahedron, 11 mm truncation of WC cubes) assemblies with octahedra cast from an MgO-based ceramic (Walker, 1991) and a graphite furnace; $P > 10$ GPa: 10/5 assemblages with precast MgO octahedra combined with pyrophyllite gaskets and a rhenium furnace (see Bertka & Fei, 1997, fig. 2a and b); at the BGI: $P \leq 10$ GPa: 18/11 assemblies with precast MgO octahedra combined with pyrophyllite gaskets and a graphite furnace; $P > 10$ GPa: 10/5 assemblages with precast MgO octahedra combined with pyrophyllite gaskets and a $LaCrO_3$ furnace. At the BGI, all experiments were conducted with precast MgO octahedra in combination with pyrophyllite gaskets. In all experiments, temperatures were measured with W3%Re–W25%Re thermocouples and both pressure and temperature were computer-controlled during the entire duration of the runs. Detailed descriptions of the GL and BGI experimental and calibration procedures have been given by Rubie *et al.* (1993) and Bertka & Fei (1997).

Table 1: Composition of starting materials

Bulk no.:	I	II	III	IV	V	VI	VII
Comp.:	MA	LIN	YI	HA	LIMA	YIHA	K-tit
TiO_2	62·1	53·9	26·4	24·5	60·7	25·4	31·4
ZrO_2	7·4	6·9	—	—	7·2	—	1·8
Cr_2O_3	18·2	17·1	41·9	31·1	15·6	36·3	36·3
Fe_2O_3	4·8	9·0	17·6	16·3	4·7	17·0	11·5
MgO	4·8	4·5	8·9	12·4	5·9	10·7	12·3
BaO	—	8·6	—	15·7	4·5	8·1	—
K_2O	2·8	—	5·2	—	1·4	2·5	6·7
$\sum$	100·0	100·0	100·0	100·0	100·0	100·0	100·0

Bulk composition VII based on averaged K-tit composition from JKW76 (see Table 3) normalized to 100%. Abbreviations are as in Table 2.

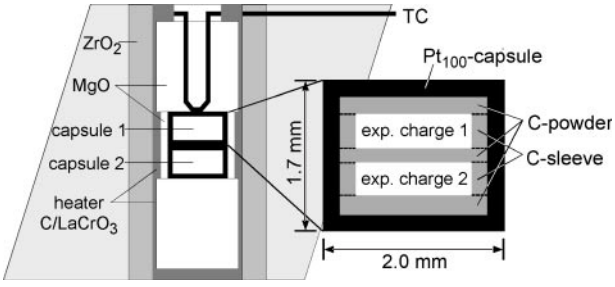

Fig. 1. Schematic cross-section through an 18/11 multianvil assembly showing the arrangement of capsules and of the experimental charges therein.

Starting materials were pre-dried at 150°C overnight, placed in 1·18 or 2·00 mm outer diameter Pt_{100} capsules and welded shut immediately. Initial experiments with this capsule material resulted in an almost complete loss of Fe to the capsule walls. Therefore, an additional inner graphite capsule (high-purity graphite ring with compressed graphite powder as bottom and lid) was used in subsequent experiments (see Table 2 and Fig. 1) to minimize Fe loss. Two experimental charges were placed in individual capsules and one capsule (10/5 assemblies) or in some cases two capsules (18/11 assemblies) were placed in a single assembly with the combined height of both capsules not exceeding 3·5 mm (Fig. 1). Attempts to place four capsules with 1·0 mm outer diameter in an 18/11 assembly were abandoned after two successful runs (JKW84, JKW43) because of problems in handling assembly parts. After the runs, recovered Pt capsules were embedded in epoxy resin and ground to expose the centre of the charges for microprobe analysis, Raman spectrometry and extraction of crystals for structure analysis. In runs at >10 GPa, the inner graphite capsule partially transformed to diamond.

Phase compositions were analysed by electron microprobe using a JEOL superprobe at the GL and a Cameca SX100 at the University of Vienna. Analytical conditions were 50 nA and 15 kV with a residence time t of 20–30 s on peak and $t/2$ s on backgrounds of the X-ray lines. Ba and Ti were analysed using the L_α and K_α lines, respectively, on a LiFH crystal. Raw counts were corrected online with the ZAF correction procedure. In the absence of information on the Fe^{2+}/Fe^{3+} ratios, Fe_{tot} is quoted as Fe^{3+} as used in the starting materials.

Phases were identified based on their chemical composition and, in part, on single-crystal structure analysis. Identification of crichtonite and magnetoplumbite phases was straightforward because of their distinctive stoichiometry and similarity to both natural counterparts and experimental run products that were identified by powder diffraction (Foley *et al.*, 1994). An identification of the phases coexisting with crichtonite and magnetoplumbite, however, often turned out to be impossible because of (1) the small grain size and modal amounts prohibiting single crystal analysis and (2) a lack of data on high-P–T phase relations and compositions of oxides in the system TiO_2–Cr_2O_3–MgO–FeO. Even in simple systems such as TiO_2–Cr_2O_3 or TiO_2–ZrO_2–Cr_2O_3–Fe_2O_3, phase relations are complex even at low pressures, with a multitude of distinctive stoichiometries and the possibility to form polysomatic series (see Flörke & Lee, 1970; Grey *et al.*, 1973). Thus, it has to be kept in mind that some of the Ti–Cr–Fe–Mg oxides listed as distinctive phases in the present study may not be phases with distinctive stoichiometry and structure, but may actually represent members of a single solid solution series with variable composition. Therefore, the number of distinctive structure types of phases coexisting with crichtonite and magnetoplumbite may actually be lower than the number of unidentified phases labelled U1–U9 described below and listed in Tables 4–7.

Single-crystal X-ray diffraction (XRD) data were collected on a Bruker Smart CCD diffractometer equipped

Table 2: Summary of experimental run conditions and products

Run no.	Bulk	Assembly	*P* (GPa)	*T* (°C)	Run time	Phases observed
JKW43	I	18/11	7·0	1300	13 h 42 min	MA + ru + $TiZrO_4$
JKW68	I	18/11 + C	7·0	1300	12 h 00 min	MA + ru + $TiZrO_4$ + U1
JKW73	I	18/11 + C	8·8	1500	10 h 00 min	MA + K-tit + Zr phase + U1 + U2
JKW78	I	18/11 + C	8·8	1600	10 h 50 min	K-tit + U2 + Zr phase + melt
JKW74	I	18/11 + C	10·0	1400	33 h 48 min	MA + K-tit + ru + $TiZrO_4$ + U1
JKW79	I	10/5 + C	11·0	1400	48 h 00 min	MA + K-tit + ru + $TiZrO_4$ + U1
JKW90	I	10/5 + C	11·0	1600	72 h 00 min	K-tit + $TiZrO_4$ + U2 + U3
JKW88	I	10/5 + C	12·0	1400	95 h 15 min	K-tit + ru + $TiZrO_4$
JKW76	I	10/5 + C	13·0	1400	48 h 00 min	K-tit + ru + $TiZrO_4$
JKW43	II	18/11	7·0	1300	13 h 42 min	LIN + ru + $TiZrO_4$
JKW68	II	18/11 + C	7·0	1300	12 h 00 min	LIN + ru + $TiZrO_4$
JKW73	II	18/11 + C	8·8	1500	10 h 00 min	LIN + ru + $TiZrO_4$
JKW81	II	18/11 + C	8·8	1600	01 h 30 min	LIN + U2 + Zr phase
JKW72	II	18/11 + C	10·0	1400	10 h 00 min	LIN + ru + $TiZrO_4$
JKW82	II	10/5 + C	11·0	1400	11 h 00 min	LIN + Ba phase 1 + Ba phase 2 + ru + $TiZrO_4$
JKW90	II	10/5 + C	11·0	1600	72 h 00 min	LIN + U2 + U3 + Zr phase
JKW88	II	10/5 + C	12·0	1400	95 h 00 min	Ba phase 1 + Ba phase 2 + ru + $TiZrO_4$ + U3
JKW83	II	10/5 + C	13·0	1400	47 h 23 min	Ba phase 1 + Ba phase 2 + ru + $TiZrO_4$ + U3
B01-6	V	18/11 + C	8·0	1300	48 h 00 min	LIMA + ru + $ZrTiO_4$
B01-9	V	18/11 + C	9·0	1150*	72 h 00 min	LIMA + ru + $ZrTiO_4$ + YI
B01-7	V	18/11 + C	9·0	1300	47 h 35 min	LIMA + ru + $ZrTiO_4$ + YI
B01-11	V	18/11 + C	9·0	1400	72 h 00 min	LIMA + ru + $ZrTiO_4$ + U4
JKW84	V	18/11 + C	10·0	1400	26 h 25 min	LIMA + ru + $ZrTiO_4$ + U4 + U5
JKW43	III	18/11	7	1300	13 h 42 min	YI + U6
JKW84	III	18/11 + C	10	1400	26 h 25 min	YI + U6
B02-12	III	10/5 + C	15	1300	72 h 00 min	YI + U2 + U6
JKW43	IV	18/11	7	1300	13 h 42 min	HA + Ba phase 3
JKW84	IV	18/11 + C	10	1400	26 h 25 min	HA + U7
B02-12	IV	10/5 + C	15	1300	72 h 00 min	HA + U7
B01-9	VI	18/11 + C	9	1150*	72 h 00 min	YIHA + HAYI + U7
B01-7	VI	18/11 + C	9	1300	47 h 35 min	YIHA + HAYI + U7 + U8
JKW84	VI	18/11 + C	10	1400	26 h 25 min	YIHA + HAYI + U7
B01-8	VI	14/8 + C	11	1300	46 h 00 min	YIHA + HAYI + U7
B01-10	VI	10/5 + C	13	1300	46 h 40 min	YIHA + HAYI + U7
B02-10	VI	10/5 + C	15	1300	72 h 00 min	YIHA + HAYI + U7 + U9
JKW86	VII	10/5 + C	13	1400	72 h 00 min	K-tit + U2

MA, mathiasite; LIN, lindsleyite; LIMA, lindsleyite–mathiasite solid solution; YI, yimengite; HA, hawthorneite; YIHA, yimengite–hawthorneite solid solution with dominant yimengite component; HAYI, yimengite–hawthorneite solid solution with dominant hawthorneite component; ru, rutile–TiO_2-II; K-tit, K–Cr-titanate; U1–U9, unidentified Ti–Cr oxides; Zr phase, Zr–Cr-titanate with fluorite-derived structure.
*Temperature estimated from power-curve because of thermocouple failure during compression; accuracy no better than approximately ±30°C.

with graphite-monochromatized MoKa radiation (λ = 0·71069 Å). A hemisphere of three-dimensional XRD data ($0° < 2\theta < 54°$) was collected with frame widths of 0·3° in ω and 30 s counting time per frame. The XRD data were analysed to locate peaks for the determination of the unit-cell parameters. The structure of a K–Cr-titanate crystal from JKW86 was solved and refined with SHELX97.

Unpolarized Raman spectra were recorded with a DilorXY spectrometer equipped with confocal optics and a Peltier-cooled CCD detector. A microscope with 100× objective was used to focus a He–Ne laser beam with 632 nm excitation wavelength onto the polished surface of experimental charges. Accumulation times from 10 to 180 s were used with a laser power of 4–8 mW to avoid beam damage. Initial attempts to record the Raman spectra of crichtonite and magnetoplumbite phases with a 514 nm Ar^+ laser resulted in an instantaneous thermal destruction of these phases.

PREVIOUS EXPERIMENTAL WORK

Both crichtonite and magnetoplumbite phases are stable at 1 atm (e.g. Chase & Wolten, 1965; Kohn & Eckart, 1965; Peterson & Grey, 1995) and, in the case of magnetoplumbite phases, represent industrially important ferrimagnetic materials such as barium ferrite $BaFe_{12}O_{19}$ (Obradors *et al.*, 1985). By comparison, only two studies have dealt with the high-pressure stability of crichtonite and magnetoplumbite phases. Podpora & Lindsley (1984) synthesized lindsleyite and mathiasite with complex natural compositions [as given by Haggerty *et al.* (1983)] at 2·0 GPa and 1300°C, and 2·2 GPa and 900°C. Foley *et al.* (1994) demonstrated the stability of end-member lindsleyite, mathiasite, yimengite, hawthorneite and solid solutions of lindsleyite–mathiasite (LIMA) and hawthorneite–yimengite (HAYI) in the system TiO_2–ZrO_2–Cr_2O_3–Fe_2O_3–MgO–BaO–K_2O in a P–T range 3–5 to 5·0 GPa and 1150–1350°C.

RESULTS

Textures and chemical homogeneity of the phases

At $P \leq 10$ GPa, crichtonite and magnetoplumbite phases usually form subhedral to rounded or lath-shaped grains with a size not exceeding ~50 μm (Fig. 2) that show strong orientation contrast in back-scattered electron (BSE) imaging (e.g. Fig. 2g). Textural equilibration is often indicated by smooth grain boundaries with regular triple grain junctions (e.g. Fig. 2a) giving a polygonal granoblastic or granuloblastic array. At pressures >10 GPa, the average grain size decreases to <20 μm and the textures become less equilibrated, with more xenomorphic grain shapes and irregular grain boundaries irrespective of run durations. All experiments except JKW78 are considered subsolidus. In JKW78 at 8·8 GPa and 1600°C, thin interstitial films along grain boundaries and irregular patches with K-rich composition were taken as an indication of the presence of small amounts of melt (Fig. 2b).

Within runs, the phase distribution is usually homogeneous. Apart from magnetoplumbite and crichtonite phases, a number of additional phases appeared in all experiments (see below). Within the stability fields of magnetoplumbite and crichtonite phases, their presence can be explained by shifts in the bulk composition as a result of: (1) partial reduction of Fe^{3+} in the starting material to Fe^{2+}; (2) loss of Fe to the Pt capsule and/or of alkalis to the graphite liner. The latter effect was observed despite careful drying of the starting materials and the graphite liners, and may also occur in alkali-rich systems at high P and T (see Konzett & Ulmer, 1999). These phases commonly form rounded to subhedral but in part euhedral grains (Fig. 2) interstitial between magnetoplumbite and crichtonite phases, and their modal amount may range from 20 to 30% to only a few grains. In some cases, they show a more zonal distribution with enrichment along the graphite–charge interface, indicating T or f_{O_2} gradients in the capsule. Because experiments of the present study are synthesis experiments and because of the notorious sluggishness of oxide equilibration, the metastable nature of some of the phases coexisting with crichtonite and magnetoplumbite cannot be ruled out.

The compositional variation of phases within runs is generally larger than that encountered in high-pressure experiments involving silicate systems, because of the sluggishness of equilibration of the oxide phases and the absence of water. The strongest within-sample variation is observed for Cr, Ti and Fe, with up to 4% relative variation with respect to the averaged values. With the exception of rutile and TiO_2-II (the α-PbO_2-structured TiO_2 modification), individual grains rarely show significant compositional zoning. Rutile or TiO_2-II may show irregular cores with variable ZrO_2 concentrations. Wherever possible, these cores were avoided during analysis. Sometimes, however, the small grain size of rutile made a partial beam overlap with these cores inevitable, which contributed to the scatter in the data (see below). It should be noted that no relation was found between the degree of textural equilibration and the homogeneity of phases. In the K_2O–BaO-bearing bulk systems, irregular variations in K_2O and BaO contents of solid-solution phases may be present. Traces of unreacted starting material are frequently present as small remnants of ZrO_2 in the cores of $ZrTiO_4$ or Zr phase grains. In a few cases (e.g. JKW88), small irregular remnants of unreacted MgO and/or $BaTiO_3$ were found in runs at $P > 10$ GPa.

Phase relations of mathiasite, lindsleyite and LIMA solid solution

In bulk composition I, mathiasite is stable at pressures between 7 and 11 GPa and temperatures between 1300° and 1500°C (Fig. 3a and Table 2). Towards high pressures, mathiasite breaks down continuously to form a K–Cr-titanate that appears at 8·8 GPa and 1500°C and

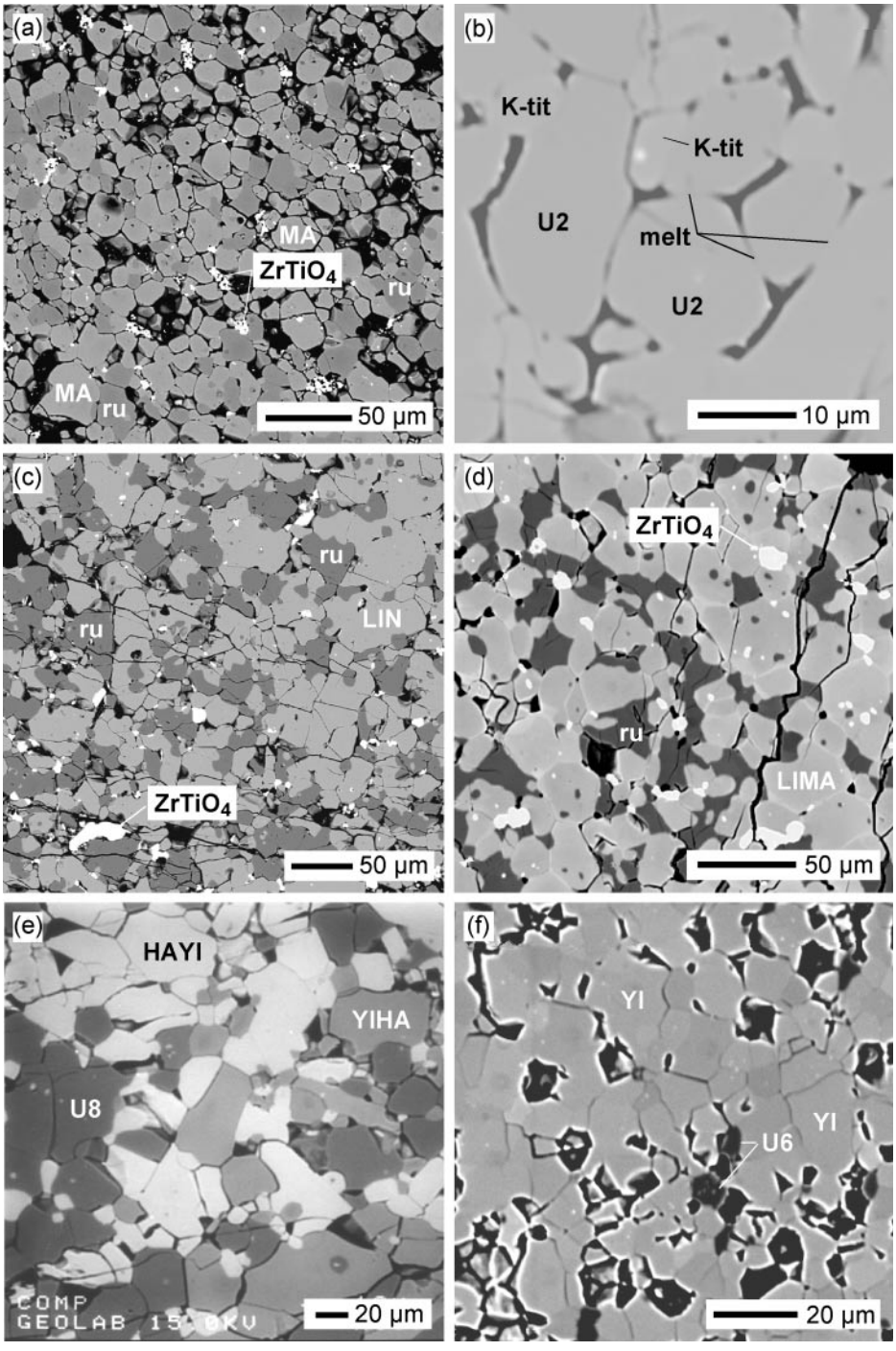

Fig. 2. BSE photomicrographs of experimental run products. (a) Mathiasite (MA); bulk composition I, 7 GPa and 1300°C; (b) formation of melt in bulk composition I present as narrow interstitial films (arrows) around grains of K–Cr-titanate (K-tit) and phase U2; (c) lindsleyite (LIN); bulk composition II, 7 GPa and 1300°C; (d) lindsleyite–mathiasite (LIMA) solid solution; bulk composition V, 7 GPa and 1300°C; (e) coexisting K- and Ba-rich hawthorneite–yimengite solid solutions (HAYI and YIHA), bulk composition VI, 10 GPa and 1400°C; (f) yimengite (YI); bulk composition IV, 15 GPa and 1300°C; (g) hawthorneite (HA), bulk composition III; 10 GPa and 1400°C. Abbreviations are as in Table 2.

coexists with mathiasite to a pressure of 11 GPa (see Konzett & Yang, 2001). In runs at 12 and 13 GPa, mathiasite is no longer stable and is replaced by the K–Cr-titanate as the only carrier of potassium. The temperature stability of mathiasite extends to 1500°C at 8·8 GPa. At this pressure, mathiasite is replaced at 1600°C by K–Cr-titanate and small (<5%) amounts of a K-rich interstitial phase that is interpreted as quenched

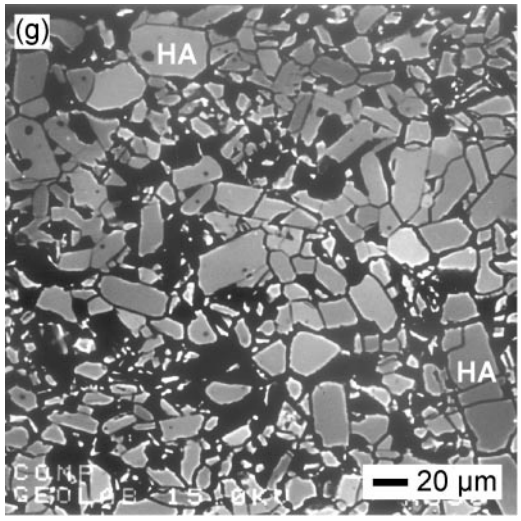

Fig. 2. Continued.

melt (Fig. 2b). Phases coexisting with mathiasite are rutile–TiO_2-II, $ZrTiO_4$, a Zr–Cr-titanate with a fluorite-derived structure (Konzett & Yang, 2001) and a number of unidentified Ti–Cr oxides.

In bulk composition II, lindsleyite is stable between 7 and 11 GPa in the temperature range 1300–1600°C (Fig. 3b and Table 2). High-pressure breakdown products of lindsleyite are two unidentified Ba–Cr-titanates (Table 4) that first appear at 11 GPa and 1400°C coexisting with lindsleyite and completely replace lindsleyite at 12 GPa and 1400°C. Unlike mathiasite, lindsleyite is still stable in runs at 1600°C. Phases coexisting with lindsleyite are rutile–TiO_2-II and $ZrTiO_4$ in addition to two unidentified Cr-titanates and the Zr–Cr-titanate also observed in bulk composition I.

Lindsleyite–mathiasite solid solutions were synthesized in the *P–T* range 7–10 GPa and 1300–1400°C from bulk composition V, to compare with the solid solution behaviour of the Ba–K-dominant members of the magnetoplumbite series (Foley *et al.*, 1994). Phases coexisting with LIMA are rutile–TiO_2-II and $ZrTiO_4$ in all runs (Fig. 2d). At 9 and 10 GPa, additional phases are present in modal amounts <2%. Only a few grains were identified even after microprobe element mapping of the entire charge. One of these phases present at 9 GPa is K rich and strongly resembles yimengite in terms of both oxide wt % and cation numbers (see Tables 5 and 6). Two other Cr–Fe–Mg-titanate phases, U4 and U5 (Table 5), remain unidentified. Because of the very small modal amounts of these phases, it is possible that they might be present in other runs using bulk composition V but were overlooked as only a single section plane through the experimental charges was examined. One run at 13 GPa and 1300°C produced very small (<5 μm) and inhomogeneous grains of a K–Ba phase interstitial between abundant rutile and $ZrTiO_4$. Despite the inhomogeneity and the likeliness of beam overlap with adjacent phases, analyses of the K–Ba phase consistently yielded only 43–46 wt % TiO_2, which is significantly lower than the TiO_2 contents of LIMA solid solutions (see below). This was taken as an indication that LIMA solid solution is no longer stable at 13 GPa and 1300°C.

Phase relations of yimengite, hawthorneite and YIHA solid solutions

Yimengite and hawthorneite were synthesized from bulk compositions III and IV at 7, 10 and 15 GPa at temperatures between 1300 and 1400°C (Fig. 2f and g). In all runs (see Table 2), one or two additional phases were found coexisting with yimengite and hawthorneite with modal abundances of <3 to 20 vol. % as determined by image analysis (Tables 6 and 7).

Attempts to synthesize 50:50 yimengite–hawthorneite solid solutions using bulk composition VI failed in the pressure range 9–15 GPa. Instead, two Ba–K phases were found in all runs (see Fig. 2e), which is consistent with results obtained by Foley *et al.* (1994). Those workers also reported two coexisting Ba–K phases in this system at 4·3 and 5·0 GPa and 1150–1350°C, and took this finding as an indication of the presence of a solvus in the system yimengite–hawthorneite. In all runs of this study using bulk composition VI, one or two phases appear in addition to the two yimengite–hawthorneite solid solutions (Fig. 2e and Table 7).

Mineral chemistry

Crichtonite phases

When normalized to 38 oxygens and assuming all Fe as Fe_2O_3 ($Fe_{tot} = Fe_2O_3$), almost all crichtonite analyses obtained from the experiments of the present study show a deviation from the ideal $AM_{21}O_{38}$ stoichiometry

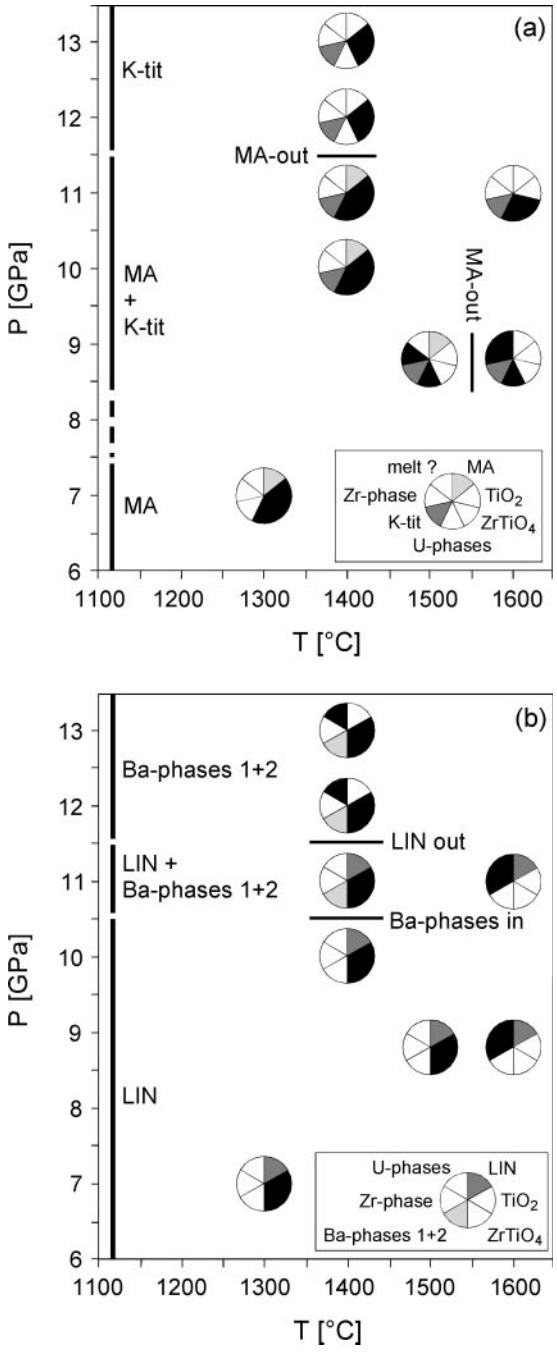

Fig. 3. Schematic *P–T* diagrams summarizing experimental results (a) for bulk compositions I and (b) for bulk composition II; phases present in the experimental charges are represented by black or grey sectors within the run symbol; phases not detected are denoted by white sectors (see inset lower right). Abbreviations are as in Table 2.

in terms of total cation as well as A-site and M-site cation sums. This variation is most pronounced for lindsleyite with $\sum$cations, $\sum$A-cations and $\sum$M-cations in the range 21·55–22·29, 0·84–1·28 and 20·39–21·40 (n = 51), respectively. The least variation was observed for experimental LIMA analyses, which cluster tightly around the ideal stoichiometric values (Fig. 4). Except for lindsleyite analyses, no correlation can be observed between pressure and the degree of non-stoichiometry. Lindsleyite shows a significant A-site cation surplus of 1·21 ± 0·04 and 1·18 ± 0·06 atoms per formula unit (a.p.f.u.) along with an M-site deficiency of 20·58 ± 0·03 and 20·43 ± 0·03 a.p.f.u. at 10 GPa and 1600°C and 11 GPa and 1600°C compared with lower-temperature runs that show A-site deficiency and M-site surplus (see Tables 3 and 4). The non-stoichiometry of crichtonite analyses is consistent with data for natural crichtonites from upper-mantle settings (Jones *et al.*, 1982; Haggerty, 1983, 1987; Haggerty *et al.*, 1983; Zhou *et al.*, 1984; Varlamov *et al.*, 1996; Wang *et al.*, 1999; Konzett *et al.*, 2000; Grégoire *et al.*, 2002) that show an even stronger variation in stoichiometric coefficients with values for $\sum$cations, $\sum$A-cations and $\sum$M-cations in the range 21·68–22·82, 0·40–1·50 and 20·67–21·84 (n = 32), respectively (see Fig. 4). It should be kept in mind, however, that an assignment of phases to the crichtonite series is usually based on the similarity of electron microprobe analyses to those of crichtonite phases and not on structure analysis. This includes data with anomalously low $\sum$A-cations in the range 0·40–0·49 reported by Varlamov *et al.* (1996).

The chemical variability of crichtonite phases synthesized in Pt capsules with graphite liners is most pronounced in the Ti and Cr contents, which always show the highest standard deviations for averaged concentrations for individual runs (Tables 3–5). Because there is no evidence for significant amounts of vacancies, at least not in runs at ≤1500°C, Ti ⇔ Cr exchange requires a coupled substitution involving mono- or divalent cations. General trends in the covariation of Cr with Ti, Mg and Fe (Fig. 5a–c) are similar for crichtonite phases, albeit with some variation in the degree of correlation, and are consistent with a substitution 2 Cr ⇔ Ti + Mg, combined with Mg ⇔ Fe^{2+} and possibly Cr ⇔ Fe^{3+}. Although Fe is present in the starting material as Fe^{3+} only, the positive correlation between Fe and Mg observed in runs using bulk compositions II and V would be consistent with some Fe^{2+} in the run products as a result of Fe reduction in the presence of graphite–diamond. The extent of Cr ⇔ Fe^{3+} exchange is difficult to estimate because the negative Cr–Fe correlation would be consistent with both 2Cr ⇔ Ti + (Mg, Fe^{2+}) and Cr ⇔ Fe^{3+}.

Crichtonites synthesized in run JKW43 without an inner graphite liner show an almost complete lack of Fe combined with much higher Mg and Cr contents compared with crichtonites from JKW68 synthesized at identical P and T conditions but in the presence of graphite–diamond (Fig. 5). The negative correlation of both Fe–Cr and Fe–Mg (Fig. 5b and c) for crichtonite

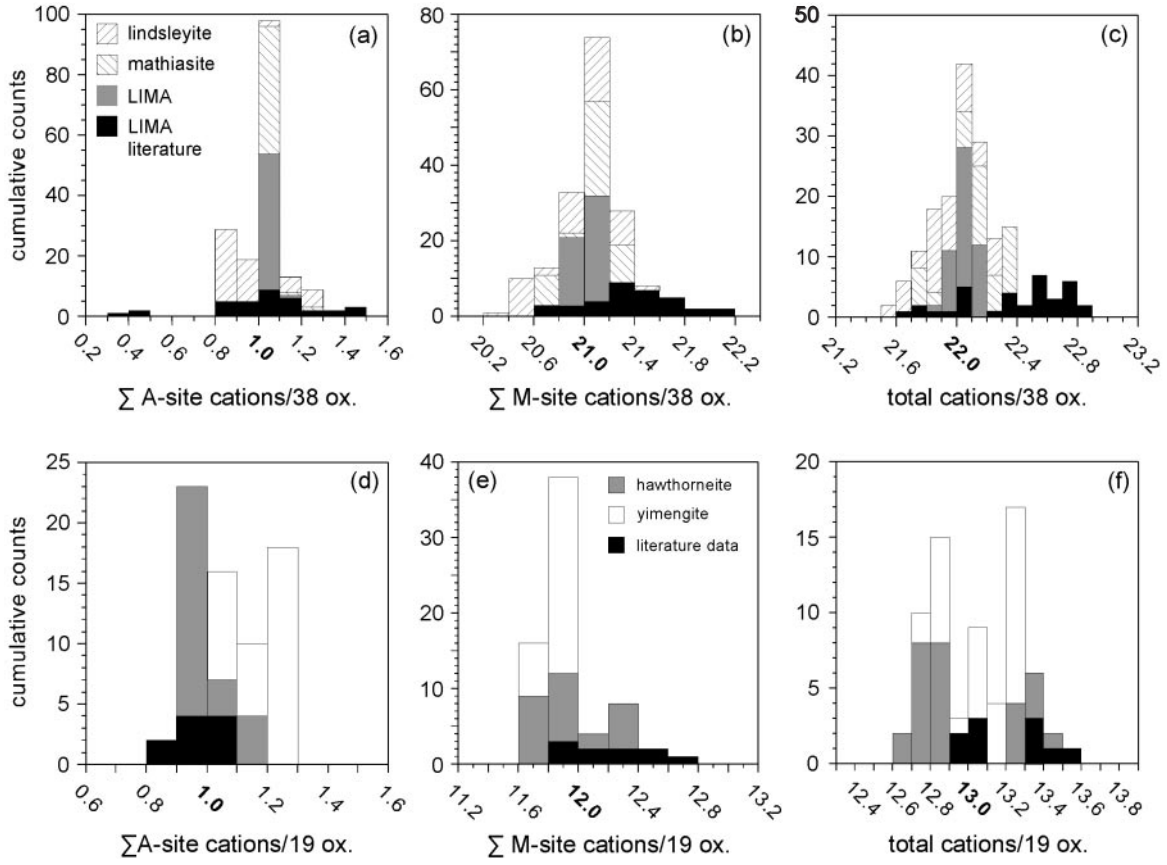

Fig. 4. (a)–(c) Distribution of cation sums for crichtonites synthesized in this study and normalized to 38 oxygens and $Fe_{tot} = Fe^{3+}$; ideal values for ∑A-site cations, ∑M-site cations and total cations are marked in bold; literature data are plotted for comparison. Sources of literature data: Jones *et al.* (1982); Haggerty (1983, 1987); Haggerty *et al.* (1983); Zhou *et al.* (1984); Varlamov *et al.* (1996); Wang *et al.* (1999); Konzett *et al.* (2000); Grégoire *et al.* (2002). (d)–(f) Distribution of cation sums for magnetoplumbites synthesized in this study and normalized to 19 oxygens and $Fe_{tot} = Fe^{3+}$; ideal values for ∑A-site cations, ∑M-site cations and total cations are marked in bold; literature data are plotted for comparison. Sources of literature data: Zhou *et al.* (1984); Haggerty *et al.* (1989); Nixon & Condliffe (1989); Sobolev *et al.* (1997); Velde (2000); Bulanova *et al.* (2004).

compositions in runs JKW43 and JKW68 could be explained by a substitution of the type $2Cr + Mg \Leftrightarrow Ti + 2Fe^{2+}$. The presence of Fe^{2+} required for this exchange would be consistent with f_{O_2} permitting Fe loss to the Pt capsule through the formation of a Pt–Fe alloy. A comparison of the Fe–Mg data (apart from direct inspection of Fe concentrations) further shows that run B02-11 must have suffered some Fe loss in spite of the presence of a graphite liner.

Apart from the Ti–Cr variation as discussed above, analyses of the LIMA solid solution are also characterized by a systematic increase in K/(Ba + K) ratios with pressure (Fig. 5d), which requires a coupled substitution involving a monovalent cation. The positive correlation between K and Ti observed for LIMA analyses (Fig. 5e) would be consistent with an exchange of the type K + Ti ⇔ Cr + (Ba + Mg). Although there is some scatter in the data, negative correlations between K and Cr and a positive correlation between Mg and Ba (Fig. 5f) would support this assumption.

The Raman spectra of mathiasite, lindsleyite and LIMA solid solution are characterized by broad bands in the wavenumber region $<800\,cm^{-1}$ (Fig. 6a). The most prominent feature is a broad and asymmetric band in the region 657–695 cm^{-1} that may be split in the case of lindsleyite into two adjacent bands at 662 and 702 cm^{-1}. Towards lower wavenumbers, bands at 543–560, 432–437, 316–324 and 201–205 cm^{-1} are present in all crichtonite phases (Fig. 6a). As a result of anisotropy, additional bands at 354 cm^{-1} in mathiasite are present only as shoulders on the 316–324 cm^{-1} bands in lindsleyite and LIMA solid solution. Similarly, bands at 243 and 248 cm^{-1} present in the LIMA and mathiasite spectra appear as shoulders only in the lindsleyite spectrum.

K–Cr-titanate

This phase is a breakdown product of mathiasite in runs with bulk composition I, and is the only carrier of potassium under subsolidus conditions apart from

Table 3: Averaged and representative electron microprobe analyses of phases in the system TiO_2–ZrO_2–Cr_2O_3–Fe_2O_3–MgO–K_2O (bulk composition I)

Experiment:	JKW43	JKW68	JKW73	JKW74	JKW79	JKW79	JKW73	JKW73	JKW78	JKW74	JKW79	JKW88	JKW90	JKW76
P (GPa):	7·0	7·0	8·8	10·0	11·0	11·0	8·8	8·8	8·8	10·0	11·0	12·0	11·0	13·0
T (°C):	1300	1300	1500	1400	1400	1400	1500	1500	1600	1400	1400	1400	1600	1400
Phase:	mathiasite						K–Cr-titanate							
No. of analyses:	10	10	8	14	1	1	2	2	6	5	6	8	7	9
TiO_2	63·4(9)	63·6(5)	66·1(7)	61·9(6)	61·8	61·4	40·1	37·4	40·5(4)	36·1(3)	34·9(4)	31·5(4)	37·5(4)	31·9(3)
ZrO_2	6·0(3)	5·8(2)	6·1(3)	5·5(1)	5·1	5·6	4·9	5·1	4·5(2)	3·4(1)	2·3(1)	1·6(2)	4·3(2)	1·8(1)
Cr_2O_3	20·2(8)	17·6(4)	16·9(4)	18·4(3)	20·5	20·3	29·7	32·8	33·6(5)	30·3(3)	34·1(6)	36·3(7)	31·1(6)	36·7(6)
Fe_2O_3*	0·3(2)	4·8(1)	3·8(1)	4·7(1)	3·8	4·0	10·2	8·9	3·5(0)	11·6(2)	11·0(3)	11·9(4)	10·3(3)	11·6(3)
MgO	7·0(2)	5·2(1)	4·3(1)	5·3(1)	5·2	5·2	10·3	9·7	11·9(3)	12·8(4)	12·8(3)	12·8(5)	10·6(2)	12·5(4)
K_2O	3·0(1)	3·0(0)	3·0(0)	3·0(0)	3·1	3·3	6·5	6·8	6·8(1)	6·7(1)	6·9(2)	6·8(1)	6·6(2)	6·8(1)
∑	99·9(5)	100·0(3)	100·2(2)	98·8(4)	99·3	99·8	101·7	100·7	100·8(5)	100·9(6)	102·0(4)	100·9(5)	100·3(7)	101·2(4)
Oxygens	38	38	38	38	38	38	12	12	12	12	12	12	12	12
Ti	13·16(14)	13·24(06)	13·68(09)	13·06(06)	12·98	12·88	2·76	2·62	2·78(2)	2·51(0)	2·40(2)	2·21(3)	2·62(2)	2·23(2)
Zr	0·80(04)	0·78(03)	0·82(04)	0·75(13)	0·69	0·76	0·22	0·23	0·20(1)	0·15(0)	0·10(1)	0·07(1)	0·19(1)	0·08(1)
Cr	4·40(20)	3·85(09)	3·68(11)	4·09(07)	4·52	4·47	2·15	2·41	2·43(4)	2·21(0)	2·47(5)	2·67(5)	2·28(3)	2·69(5)
Fe^{3+}	0·06(03)	1·00(02)	0·80(02)	1·00(02)	0·80	0·85	0·70	0·62	0·24(0)	0·81(1)	0·76(2)	0·84(3)	0·72(2)	0·81(2)
Mg	2·86(06)	2·15(03)	1·77(03)	2·21(02)	2·14	2·15	1·40	1·35	1·62(0)	1·76(4)	1·75(3)	1·78(7)	1·47(3)	1·73(4)
K	1·07(02)	1·07(01)	1·05(01)	1·08(01)	1·09	1·20	0·76	0·81	0·80(1)	0·79(1)	0·80(2)	0·81(1)	0·78(2)	0·81(1)
∑	22·34(03)	22·09(02)	21·79(01)	22·18(03)	22·22	22·31	7·98	8·04	8·08(1)	8·23(1)	8·28(2)	8·37(3)	8·07(1)	8·35(1)
∑A-cations	1·07(02)	1·07(01)	1·05(01)	1·08(10)	1·09	1·20								
∑M-cations	21·28(02)	21·02(02)	20·74(02)	21·11(01)	21·13	21·11								

Experiment:	JKW43	JKW68	JKW74	JKW79	JKW88	JKW76	JKW74	JKW79	JKW90	JKW76
P (GPa):	7·0	7·0	10·0	11·0	12·0	13·0	10·0	11·0	11·0	13·0
T (°C):	1300	1300	1400	1400	1400	1400	1400	1400	1600	1400
Phase:	ru	ru	ru	TiO_2-II	TiO_2-II	TiO_2-II	$ZrTiO_4$			
No. of analyses:	6	6	1	1	1	4	1	1	3	4
TiO_2	83·4(5)	85·8(11)	84·4	79·9	89·1	83·3(9)	31·9	32·1	30·6(4)	33·5(3)
ZrO_2	3·1(4)	1·7(3)	2·9	4·5	2·5	3·4(9)	68·4	65·3	68·2(9)	64·8(3)
Cr_2O_3	11·7(2)	9·7(2)	9·1	11·8	7·5	10·0(9)	0·3	0·3	0·4(2)	0·4(0)
Fe_2O_3*	b.d.	0·6(0)	0·7	2·5	0·6	1·7(3)	0·2	0·2	0·2(1)	0·2(0)
MgO	0·4(0)	0·4(0)	0·3	1·4	0·1	0·9(2)	b.d.	b.d.	b.d.	b.d.
K_2O	b.d.	b.d.	b.d.	b.d.	b.d.	b.d.	b.d.	b.d.	b.d.	b.d.
∑	98·7(4)	98·2(8)	97·5	100·0	99·8	99·3(5)	100·8	97·94	99·4(6)	99·0(4)

Table 3: continued

Experiment:	JKW43	JKW68	JKW74	JKW79	JKW88	JKW76	JKW74	JKW79	JKW90	JKW76
P (GPa):	7·0	7·0	10·0	11·0	12·0	13·0	10·0	11·0	11·0	13·0
T (°C):	1300	1300	1400	1400	1400	1400	1400	1400	1600	1400
Phase:	ru	ru	ru	TiO_2-II	TiO_2-II	TiO_2-II	$ZrTiO_4$			
No. of analyses:	6	6	1	1	1	4	1	1	3	4
Oxygens	1·93	1·94	1·94	1·90	1·96	1·93	4	4	4	4
Ti	0·85(0)	0·87(0)	0·87	0·80	0·90	0·84(1)	0·84	0·86	0·81(1)	0·88(0)
Zr	0·02(0)	0·01(0)	0·02	0·03	0·02	0·02(1)	1·16	1·14	1·17(2)	1·10(0)
Cr	0·13(0)	0·10(0)	0·10	0·12	0·08	0·11(1)	—	—	0·02(0)	0·02(0)
Fe^{3+}	—	0·01(0)	0·01	0·02	0·01	0·02(0)	—	—	—	—
Mg	0·01(0)	0·01(0)	0·01	0·03	—	0·02(0)	—	—	—	—
K	—	—	—	—	—	—	—	—	—	—
∑	1·00	1·00	1·00	1·00	1·00	1·00	2·00	2·00	2·00(0)	2·00(0)

Experiment:	JKW68	JKW74	JKW73	JKW78	JKW90	JKW90	JKW78	
P (GPa):	7	10	8·8	8·8	11·0	11·0	8·8	
T (°C):	1300	1400	1500	1600	1600	1600	1600	
Phase:	U1	U1	U2	U2	U3	U3	Zr phase	melt?
No. of analyses:	1	1	6	8	7	1	5	1
TiO_2	39·9	40·1	71·5(7)	72·4(5)	72·4(9)	43·8	53·0(5)	67·7
ZrO_2	0·6	0·6	7·7(7)	6·4(1)	8·5(5)	11·7	29·4(5)	0·6
Cr_2O_3	35·8	31·3	16·3(13)	16·9(1)	13·8(8)	24·5	9·4(1)	17·1
Fe_2O_3*	13·0	14·4	2·3(3)	1·0(1)	3·1(2)	11·0	2·1(0)	0·2
MgO	12·3	14·4	2·2(1)	2·9(1)	2·2(4)	10·0	6·9(2)	0·3
K_2O	b.d.	b.d.	b.d.	b.d.	b.d.	b.d.	b.d.	12·7
∑	101·6	100·7	100·1(7)	99·6(6)	100·0(5)	100·9	100·9(6)	98·6
Oxygens							8	
Ti							2·41(1)	
Zr							0·87(1)	
Cr							0·45(1)	
Fe^{3+}							0·09(0)	
Mg							0·62(2)	
K							—	
∑							4·45(1)	

*Total Fe expressed as Fe_2O_3 as used in the starting material.
Numbers in parentheses represent standard deviation. Abbreviations are as in Table 2. b.d., below detection limit.

Table 4: Averaged electron microprobe analyses of phases in the system TiO_2–ZrO_2–Cr_2O_3–Fe_2O_3–MgO–BaO (bulk composition II)

Experiment:	JKW43	JKW68	JKW73	JKW81	JKW72	JKW82	JKW90	JKW82		JKW88		JKW83	
P (GPa):	7·0	7·0	8·8	8·8	10·0	11·0	11·0	11·0		12·0		13·0	
T (°C):	1300	1300	1500	1600	1400	1400	1600	1400		1400		1400	
Phase:	lindsleyite							Ba phase 1	Ba phase 2	Ba phase 1	Ba phase 2	Ba phase 1	Ba phase 2
No. of analyses:	6	10	11	6	5	7	7	3	4	5	4	9	3
TiO_2	55·6(7)	55·6(5)	57·4(3)	58·7(7)	55·2(5)	55·3(5)	59·5(6)	52·4(1)	50·2(4)	56·3(5)	51·4(9)	53·1(5)	51·0(3)
ZrO_2	5·6(1)	5·1(2)	5·3(1)	2·1(1)	4·4(1)	4·3(3)	3·0(2)	0·9(1)	1·1(0)	0·4(0)	0·5(1)	0·5(1)	0·5(0)
Cr_2O_3	20·8(7)	17·7(5)	17·2(3)	19·8(9)	17·6(2)	17·2(3)	17·0(2)	15·8(3)	20·0(3)	16·4(4)	21·4(14)	17·2(5)	21·2(3)
Fe_2O_3*	2·8(4)	8·5(6)	8·2(3)	5·6(4)	9·6(1)	9·3(2)	7·6(2)	6·1(2)	8·8(1)	4·4(1)	8·4(7)	4·9(2)	8·1(1)
MgO	6·6(3)	4·7(1)	4·3(1)	3·3(1)	4·7(1)	5·3(2)	2·8(1)	3·2(1)	4·0(1)	1·4(2)	3·1(1)	2·6(1)	3·8(0)
BaO	7·7(1)	7·7(2)	7·7(1)	10·5(3)	7·6(3)	7·8(2)	10·2(5)	20·9(3)	15·8(3)	21·3(6)	16·1(9)	21·6(3)	15·5(3)
∑	99·1(3)	99·3(5)	100·1(4)	100·0(4)	99·0(3)	99·3(4)	100·1(6)	99·2(6)	99·9(4)	100·2(9)	100·9(5)	99·8(6)	99·9(4)
Oxygens	38	38	38	38	38	38	38						
Ti	12·24(9)	12·30(6)	12·56(4)	12·99(9)	12·24(6)	12·22(8)	13·14(8)						
Zr	0·79(1)	0·73(2)	0·76(2)	0·30(1)	0·63(2)	0·61(4)	0·43(2)						
Cr	4·82(10)	4·11(11)	3·95(9)	4·61(20)	4·10(7)	4·01(7)	3·96(4)						
Fe^{3+}	0·62(9)	1·89(14)	1·79(6)	1·24(8)	2·12(1)	2·06(4)	1·68(5)						
Mg	2·89(10)	2·05(5)	1·88(2)	1·44(3)	2·05(2)	2·34(10)	1·23(2)						
Ba	0·89(1)	0·89(2)	0·88(1)	1·21(4)	0·88(4)	0·91(3)	1·18(6)						
∑	22·25(3)	21·97(3)	21·82(1)	21·79(4)	22·02(3)	22·14(6)	21·61(4)						
∑A-cations	0·89(1)	0·89(2)	0·88(1)	1·21(4)	0·88(4)	0·91(3)	1·18(6)						
∑M-cations	21·36(3)	21·08(4)	20·93(1)	20·58(3)	21·14(3)	21·24(6)	20·44(3)						

Table 4: continued

Experiment:	JKW43	JKW68	JKW72	JKW82	JKW88	JKW76	JKW81	JKW90	JKW72	JKW88	JKW81	JKW90	JKW90	JKW88	JKW83
P (GPa):	7·0	7·0	10·0	11·0	12·0	13·0	8·8	11·0	10·0	12·0	8·8	11·0	11·0	12·0	13·0
T (°C):	1300	1300	1400	1400	1400	1400	1600	1600	1400	1400	1600	1600	1600	1400	1400
Phase:	ru	ru	ru	TiO_2-II	TiO_2-II	TiO_2-II	Zr phase	Zr phase	$ZrTiO_4$	$ZrTiO_4$	U2	U2	U3	U3	U3
No. of analyses:	4	1	1	1	1	1	5	1	1	1	4	1	1	3	1
TiO_2	80·8(5)	83·5	79·8	88·7	91·8	86·0	57·6(5)	47·8	32·0	34·7	73·6(6)	74·2	42·5	41·7(4)	41·7
ZrO_2	4·3(4)	3·7	7·4	1·2	2·0	2·9	21·0(9)	33·9	67·7	64·8	5·2(2)	8·5	11·9	10·9(5)	14·7
Cr_2O_3	13·3(1)	10·8	9·7	6·2	4·5	7·9	9·1(8)	5·9	0·3	0·2	14·6(3)	11·2	20·6	19·1(4)	16·9
Fe_2O_3*	0·3(0)	1·4	2·3	2·2	0·8	1·6	8·2(6)	8·4	0·4	0·3	4·7(1)	5·2	17·4	19·5(7)	16·9
MgO	0·6(0)	0·6	0·7	0·8	0·2	0·5	5·5(3)	4·2	b.d.	b.d.	2·5(1)	1·7	7·9	9·5(1)	9·9
BaO	b.d.	b.d.	b.d.	b.d.	b.d.	b.d.	b.d.	b.d.	b.d.	b.d.	b.d.	b.d.	b.d.	b.d.	b.d.
$\sum$	99·3(6)	100·0	99·9	99·1	99·4	98·9	101·6(8)	100·2	100·4	100·0	100·8(9)	100·8	100·4	100·7(8)	100·1
Oxygens	1·92	1·93	1·92	1·94	1·97	1·94	8	8	4	4					
Ti	0·82(0)	0·84	0·81	0·89	0·93	0·87	2·61(2)	2·25	0·84	0·90					
Zr	0·03(0)	0·02	0·05	0·01	0·01	0·02	0·62(2)	1·04	1·15	1·09					
Cr	0·14(0)	0·11	0·10	0·07	0·05	0·08	0·43(4)	0·29	0·01	0·01					
Fe^{3+}	—	0·01	0·02	0·02	0·01	0·02	0·41(3)	0·40	0·01	0·01					
Mg	0·01(0)	0·01	0·01	0·02	0·01	0·01	0·49(3)	0·39	—	—					
Ba	—	—	—	—	—	—	—	—	—	—					
$\sum$	1·00	1·00	1·00	1·00	1·00	1·00	4·56(2)	4·37	2·00	2·01					

*Total Fe expressed as Fe_2O_3.
Numbers in parentheses represent standard deviation. Abbreviations are as in Table 2.

Table 5: Averaged electron microprobe analyses of phases in the system TiO_2–ZrO_2–Cr_2O_3–Fe_2O_3–MgO–BaO–K_2O (bulk composition V)

Experiment:	B02-11	B01-6	B01-9	B01-7	B01-11	JKW84
P (GPa):	7·0	8·0	9·0	9·0	9·0	10·0
T (°C):	1300	1300	1150[1]	1300	1400	1400
Phase:	LIMA					
No.of analyses:	12	10	7	8	8	11
TiO_2	61·3(8)	59·5(8)	62·3(10)	61·9(7)	61·6(4)	64·3(5)
ZrO_2	5·8(3)	4·6(4)	4·4(3)	5·0(3)	5·6(2)	5·0(1)
Cr_2O_3	17·3(9)	17·6(9)	15·4(9)	15·2(7)	16·6(4)	15·2(5)
Fe_2O_3*	2·5(3)	4·7(3)	5·1(1)	5·0(1)	3·9(5)	4·1(3)
MgO	6·7(1)	6·3(2)	6·3(2)	6·4(2)	6·0(1)	6·0(1)
BaO	6·4(4)	5·9(5)	5·9(8)	5·4(5)	5·8(2)	4·9(4)
K_2O	0·9(1)	1·1(1)	1·1(2)	1·2(1)	1·1(1)	1·4(1)
$\sum$	100·8(4)	99·6(5)	100·3(7)	100·1(3)	100·6(2)	100·9(3)
Oxygens	38	38	38	38	38	38
Ti	13·05(13)	12·84(13)	13·26(14)	13·19(11)	13·12(7)	13·50(7)
Zr	0·80(4)	0·64(5)	0·61(3)	0·68(4)	0·77(2)	0·69(2)
Cr	3·87(21)	3·99(20)	3·44(21)	3·41(16)	3·72(9)	3·36(11)
Fe^{3+}	0·52(7)	1·01(6)	1·09(2)	1·07(3)	0·84(10)	0·86(7)
Mg	2·83(5)	2·67(9)	2·64(5)	2·71(7)	2·53(4)	2·51(6)
Ba	0·71(5)	0·66(6)	0·66(9)	0·60(6)	0·64(2)	0·54(4)
K	0·32(3)	0·40(5)	0·38(6)	0·44(5)	0·40(3)	0·49(5)
$\sum$	22·11(2)	22·22(3)	22·06(4)	22·11(2)	22·03(2)	21·95(3)
$\sum$A-cations	1·03(2)	1·06(2)	1·04(4)	1·04(2)	1·04(1)	1·03(1)
$\sum$M-cations	21·08(2)	21·15(3)	21·03(4)	21·06(2)	20·99(1)	20·92(2)
K/(K + Ba)	0·31(3)	0·38(5)	0·37(7)	0·42(5)	0·38(2)	0·48(4)

Table 5: continued

Experiment:	B02-11	B01-6	B01-9	B01-7	B01-11	B01-10	B02-11	B01-6	B01-7	B01-11	B01-10	B01-9	B01-7	B01-11	JKW84	JKW84	JKW84
P (GPa):	7·0	8·0	9·0	9·0	9·0	13·0	7·0	8·0	9·0	9·0	13·0	9·0	9·0	9·0	10·0	10·0	10·0
T (°C):	1300	1300	1150[1]	1300	1400	1400	1300	1300	1300	1400	1300	1150[1]	1300	1400	1400	1400	1400
Phase:	ru	ru	TiO_2-II?	ru	ru	TiO_2-II	$ZrTiO_4$					yimengite		U4	U4	ilm[2]	U5
No. of analyses:	5	3	1	3	5	4	3	3	3	1	1	1	1	1	1		1
TiO_2	84·9(7)	85·5(2)	94·3	86·6(3)	86·5(4)	90·7(13)	30·5(8)	30·0(9)	30·6(9)	31·1	33·4	32·8	34·3	48·5	49·6	49·3	48·7
ZrO_2	3·7(3)	1·9(5)	0·7	2·1(2)	3·9(2)	1·5(6)	68·1(12)	69·5(10)	68·4(11)	67·7	67·4	1·7	2·6	1·0	0·7	nd	11·4
Cr_2O_3	9·8(2)	8·9(4)	2·5	8·1(2)	7·5(2)	5·3(6)	0·2(0)	0·3(0)	0·2(0)	0·3	0·3	36·8	34·3	22·1	20·6	16·2	16·4
Fe_2O_3*	0·3(0)	0·9(0)	1·0	0·8(0)	0·5(1)	0·6(1)	0·2(0)	0·2(0)	0·2(0)	0·2	0·2	10·3	9·9	12·5	13·9	21·2	10·8
MgO	0·4(0)	0·6(0)	0·6	0·6(0)	0·3(0)	0·4(0)	b.d.	b.d.	b.d.	b.d.	b.d.	13·5	13·0	18·0	17·5	14·2	14·0
BaO	b.d.	b.d.	b.d.	b.d.	b.d.	b.d.	b.d.	b.d.	b.d.	b.d.	b.d.	0·5	0·4	b.d.	b.d.	n.d.	b.d.
K_2O	b.d.	b.d.	b.d.	b.d.	b.d.	b.d.	b.d.	b.d.	b.d.	b.d.	b.d.	6·0	5·6	b.d.	b.d.	n.d.	b.d.
$\sum$	99·0(5)	98·4(3)	99·7	98·9(2)	99·2(5)	98·6(2)	99·1(7)	100·2(2)	99·4(2)	99·3	101·3	101·6	100·1	102·1	102·3	100·9	101·3
Oxygens	1·94	1·94	1·97	1·94	1·95	1·96	2	2	2	2	2	19	19	2 cat. + 3 ox.			
Ti	0·86(0)	0·87(0)	0·85	0·88(0)	0·88(0)	0·92(1)	0·81(2)	0·79(2)	0·81(2)	0·82	0·86	3·60	3·80	0·80	0·82	0·84	
Zr	0·02(0)	0·01(0)	0·01	0·01(0)	0·03(0)	0·01(0)	1·18(2)	1·20(2)	1·18(2)	1·16	1·13	0·12	0·19	0·01	0·01	—	
Cr	0·10(0)	0·10(0)	0·03	0·09(0)	0·08(0)	0·06(1)	0·01(0)	0·01(0)	0·01(0)	0·01	0·01	4·24	3·99	0·38	0·36	0·29	
Fe^{3+}	—	0·01(0)	0·01	0·01(0)	0·01(0)	0·01(0)	0·01(0)	0·01(0)	0·01(0)	0·01	0·01	1·13	1·10	0·00	0·00	0·01	
Fe^{2+}	—	—	—	—	—	—	—	—	—	—	—	—	—	0·22	0·26	0·36	
Mg	0·01(0)	0·01(0)	0·01	0·01(0)	0·01(0)	0·01(0)	—	—	—	—	—	2·93	2·85	0·59	0·58	0·48	
Ba	—	—	—	—	—	—	—	—	—	—	—	0·03	0·03	—	—	—	
														2·00	2·02	1·98[3]	

[1]See Table 2 for explanation.
[2]Ilmenite (analysis MW38-64) reported by Stachel *et al*. (1998) as inclusion in diamond; the analysis also contains 1·0 wt % Al_2O_3, 0·2 wt % MnO and 0·4 wt % NiO; Fe recalculated to Fe^{3+}.
[3]$\sum$cat = 2·00 with Ni and Al.
*Total Fe expressed as Fe_2O_3.
Numbers in parentheses represent standard deviation. Abbreviations are as in Table 2. n.d., not determined.

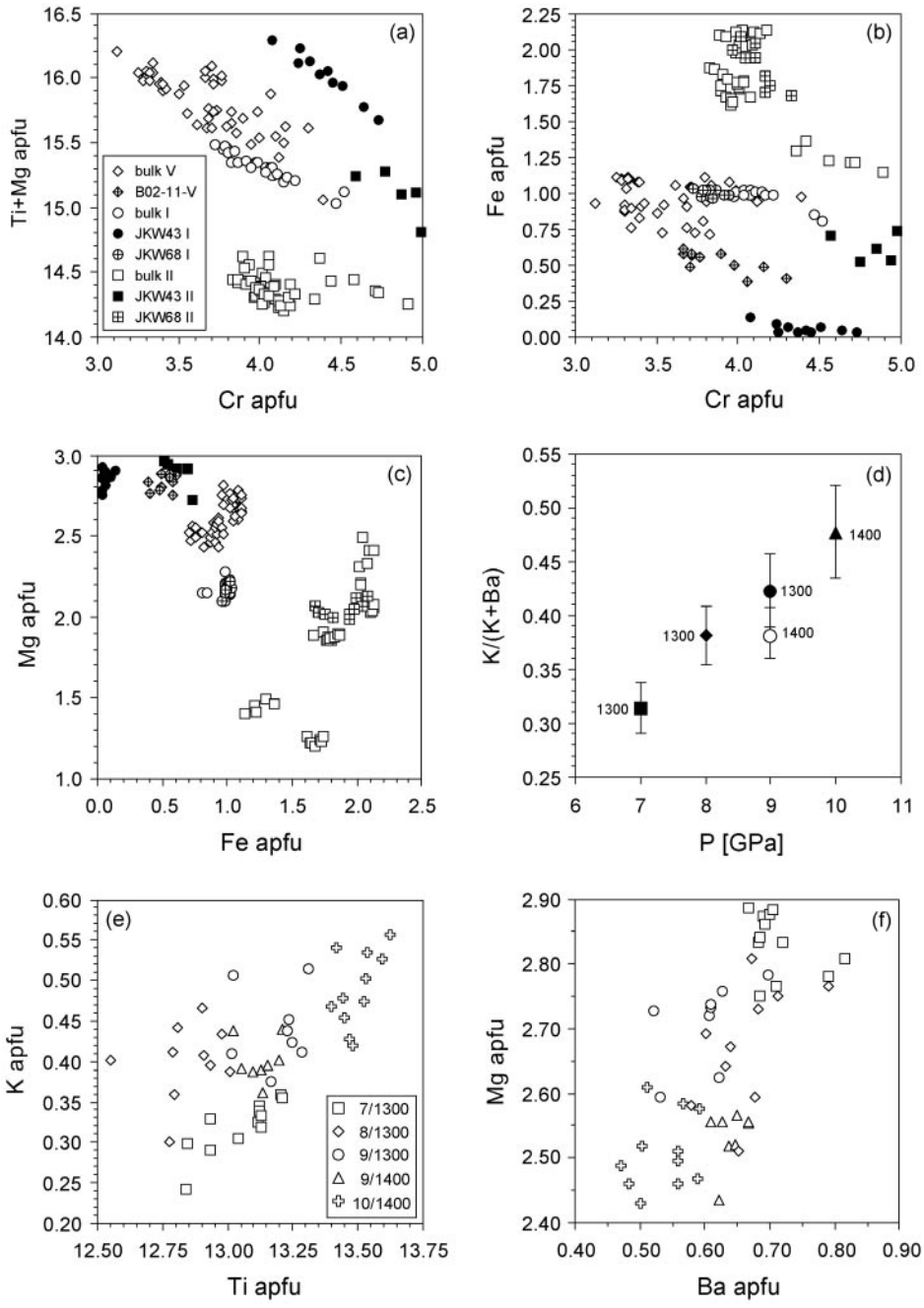

Fig. 5. Compositional variation of crichtonite phases synthesized in this study. (a) Ti + Mg vs Cr atoms per formula unit (a.p.f.u.); (b) Fe (Fe_{tot} = Fe^{3+}) vs Cr; (c) Mg vs Fe; (d) K/(K + Ba) vs pressure (GPa) for lindsleyite–mathiasite solid solutions (LIMA); numbers next to plot symbols are experimental temperatures; (e) K vs Ti and (f) Mg vs Ba for LIMA; plot symbols are given in insets in (a) and (e); roman numbers refer to bulk compositions listed in Table 1; crichtonite compositions from runs JKW43 and JKW68 are marked to show the difference in composition due to the absence of a graphite liner (see Table 2).

mathiasite in this system. Compared with mathiasite, the K–Cr-titanate contains much less TiO_2 (31–37 wt %) and more Cr_2O_3 (30–37 wt %), and twice as much K_2O (6·5–7·0 wt %).

The XRD study on a K–Cr-titanate single crystal from JKW86 (bulk VII) shows that it possesses an unreported structure with the unit cell parameters $a = 9{\cdot}175(2)$ Å, $c = 2{\cdot}879(1)$ Å, $V = 209{\cdot}9(1)$ Å^3, and space group $P6_3/m$. The crystal structure of this K–Cr-titanate phase contains three cationic sites M1, M2 and M3, which are occupied by ($Ti^{4+} + Zr^{4+} + Cr^{3+} + Fe^{3+}$), Mg^{2+} and K^+, respectively. Its main feature is double chains of M1 octahedra,

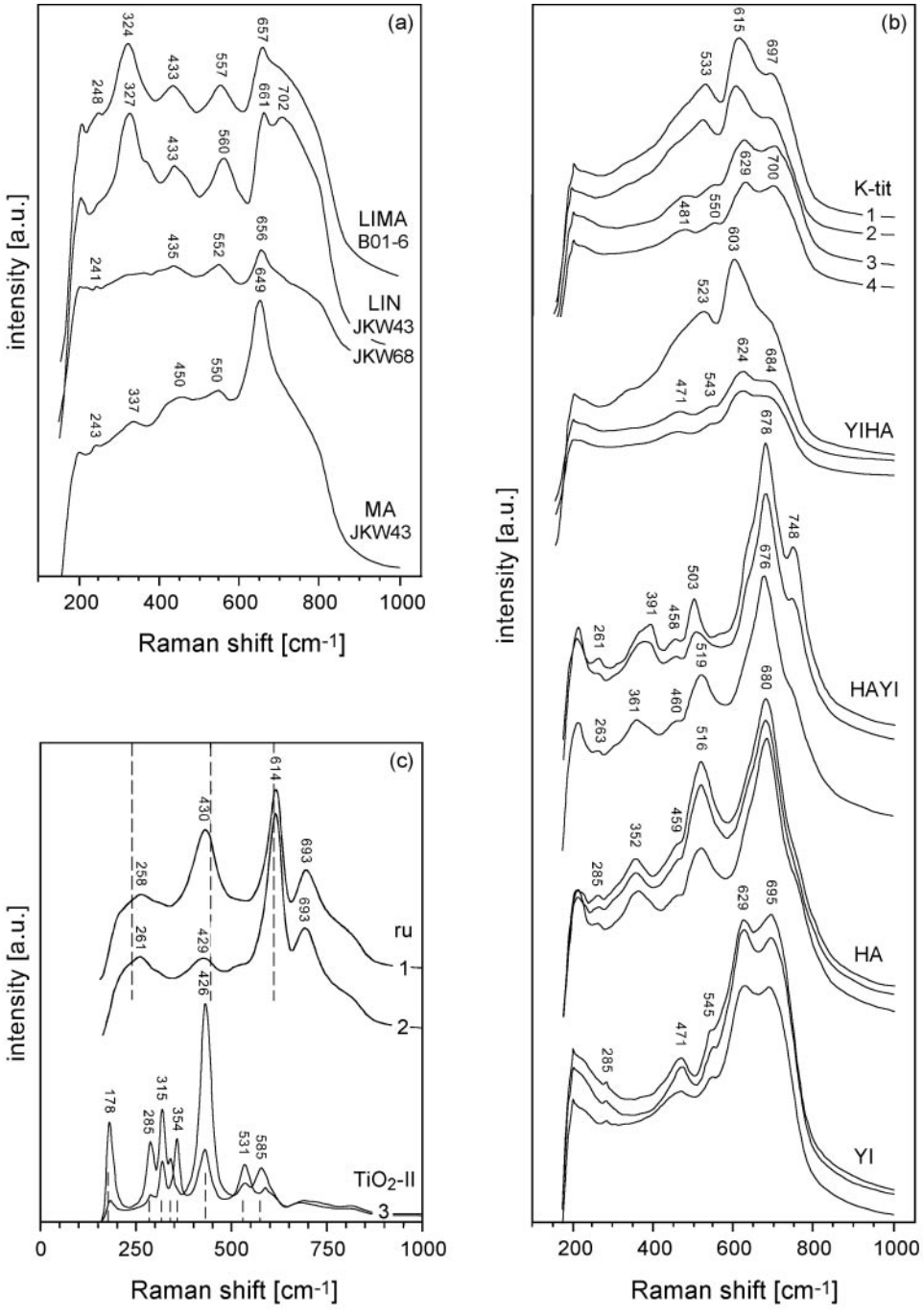

Fig. 6. Unpolarized Raman spectra (excitation wavelength 632 nm) of experimental run products. (a) Phases of the crichtonite group; (b) phases of the magnetoplumbite group and the K–Cr-titanate; spectra 1, 3, and 4 from run JKW88; spectrum 2 from run JKW76; (c) TiO_2 modifications: spectra 1 and 2 from JKW43 (bulk I) and B01-6 (bulk V) containing 11·7 and 8·9 wt % Cr_2O_3, respectively; spectra 3: TiO_2-II from JKW88 (bulk II) containing 5·2 wt % Cr_2O_3; dashed lines denote positions of bands in pure synthetic rutile and TiO_2-II (Linde & DeCarli, 1969).

which consist of two adjacent single chains that share octahedral edges running parallel to the *c*-axis. The double chains link corners with each other to form a framework with two types of tunnels, one occupied by M2 cations and the other by M3 (Fig. 7). A more comprehensive description of the structure will be reported elsewhere.

On a 12 oxygen basis suggested by the structure analysis, K–Cr-titanate analyses are characterized by a significant variation in $\sum R^{2+} + R^{3+}$ and $\sum R^{4+}$, ranging

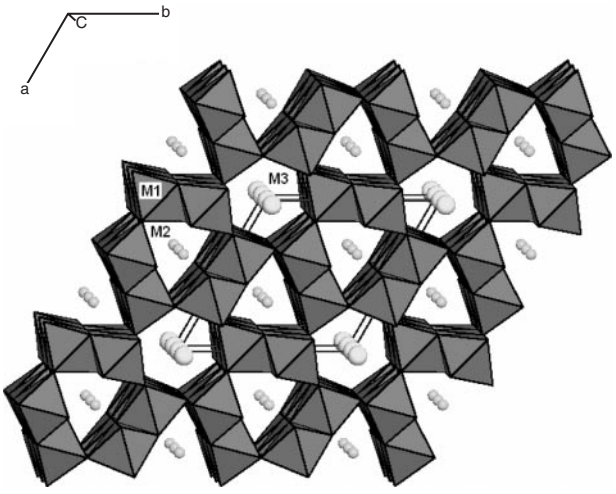

Fig. 7. Structure of the K–Cr-titanate in a perspective view down the *c*-axis; large cation positions in hexagonal tunnels are occupied by K, small cation positions in triangular tunnels are occupied by Mg (see also description in text).

from 4·29 to 5·29 and from 2·28 to 2·99 a.p.f.u., respectively (Fig. 8a, Table 3). Total cation sums, too, show a variation in the range 8·08–8·37 a.p.f.u. At constant temperature, both $\sum$total cations and $\sum R^{2+} + R^{3+}$ tend to increase, whereas $\sum R^{4+}$ decreases. Cation sums for JKW90 (11 GPa and 1600°C) deviate from the trend, with the possibility that high- and low-temperature runs at 1600 and 1400°C follow two separate trends (Fig. 8a). The large cation position, on the other hand, does not show any significant variation with pressure or temperature, and ranges between $0{\cdot}78 \pm 0{\cdot}02$ and $0{\cdot}81 \pm 0{\cdot}01$ a.p.f.u. (Table 3).

As was the case for crichtonite phases, major variations in K–Cr-titanate compositions are observed in Cr and Ti with an increase in Cr with increasing pressure (Fig. 8b). Possible exchange mechanisms to account for the observed compositional variation of K–Cr-titanate are more difficult to evaluate compared with crichtonite phases because of the variability of cation sums with the possibility of vacancies being involved. Nevertheless, element covariations (e.g. Fig. 8b–d) would be consistent with exchange mechanisms of the form $2\,R^{3+} \Leftrightarrow R^{4+} + R^{2+}$. Again, some reduction of Fe^{3+} is likely to have occurred in the presence of graphite–diamond. A negative correlation of Fe with Ti (Fig. 8d) and positive correlations with Mg and Cr would be consistent with the presence of both Fe^{2+} and Fe^{3+} involved in $2\,Cr \Leftrightarrow Ti + (Mg + Fe^{2+})$ and $2\,(Cr + Fe^{3+}) \Leftrightarrow Ti + Mg$. Clearly, in the absence of Mössbauer data on Fe^{2+}/Fe^{3+} ratios, these considerations must remain speculative.

Rutile–TiO_2-II

The most common phase accompaying crichtonite and magnetoplumbite phases is rutile or its high-pressure equivalent TiO_2-II possessing α-PbO_2 structure (Linde & DeCarli, 1969). It always contains significant amounts of Cr, Zr and Fe, with Cr being the major impurity. The maximum observed concentrations of minor elements in rutile are 14·6 wt % Cr_2O_3, 7·3 wt % ZrO_2 and 2·3 wt % Fe_2O_3 (Tables 3–5). The rutile–TiO_2-II transition, which passes through 6·5 GPa and 1000°C and 11·0 GPa and 1500°C (Withers *et al.*, 2003, and references therein), does not have an obvious influence on the minor element contents of TiO_2 as there are no discontinuities in element correlations for TiO_2.

In the absence of pentavalent cations, the substitution of trivalent cations such as Cr or Fe^{3+} requires a shift in rutile composition towards $CrO_{1·5}$ and $FeO_{1·5}$, thus producing a non-stoichiometric rutile with a composition TiO_{2-x} (Dirstine & Rosa, 1979). Whereas Zr occupies Ti lattice positions, the incorporation of Cr is thought to take place on unoccupied octahedral voids (= interstitial) of the rutile structure, introducing local lattice defects with corundum-type structure according to $2\,Ti^{4+} + O^{2-} \Leftrightarrow 2\,(Cr^{3+}, Fe^{3+}) + v_O$ (Flörke & Lee, 1970); charge compensation is ensured by the introduction of oxygen vacancies (Dirstine & Rosa, 1979). In spite of its chemical simplicity, the system Ti–Cr–O is highly complex in terms of crystallographic structures and discrete compounds encountered (Flörke & Lee, 1970; Gibb & Anderson, 1972). According to Gibb & Anderson (1972), the rutile structure *sensu stricto* is stable with ~0–5 mol % $CrO_{1·5}$, whereby Cr substitution leads to the introduction of localized corundum-type structure defects. Between ~5 and 15 mol % $CrO_{1·5}$, anion sites are removed by crystallographic shear to achieve charge compensation, and for $CrO_{1·5}$ concentrations in the range >15 to <50 mol %, a series of discrete phases with a general formula $Cr_2Ti_{n-2}O_{2n-1}$ with $n = 6$–12 becomes stable (Fig. 9). At >50 mol % $CrO_{1·5}$, the system is saturated with respect to Cr_2O_3 (Flörke & Lee, 1970; Gibb & Anderson, 1972). The introduction of ZrO_2 and Fe_2O_3 leads to additional complexities because for suitable Cr:Fe and Ti:Zr ratios, the system Cr_2O_3–Fe_2O_3–TiO_2–ZrO_2 contains a series of phases with a general formula $(Cr,Fe)_{2p}(Ti,Zr)_{p+2q}O_{5p+4q}$ or $pM_3O_5{\cdot}qM_2O_4$ with $p = 1$–4 and $q = 0$–5, which can be represented as polysomatic intergrowths [i.e. intergrowths of distinct structure modules in various porportions; see Thompson (1978)] of V_3O_5 and α-PbO_2 structure types (Grey *et al.*, 1973) (Fig. 9). It should be noted that the crystallographic characterization of TiO_2–Cr_2O_3 solid solutions is based on 1 atm experiments and that the distinction of compositional fields with characteristic structures (i.e. rutile *sensu stricto*, crystallographic shear) is not necessarily valid for high pressures.

In the rutiles of the present study, combined $TiO_2 + ZrO_2$ is always ≥82 wt % and negatively correlated with Cr close to a 1:1 exchange line. $(Cr, Fe^{3+})O_{1·5}$ does not

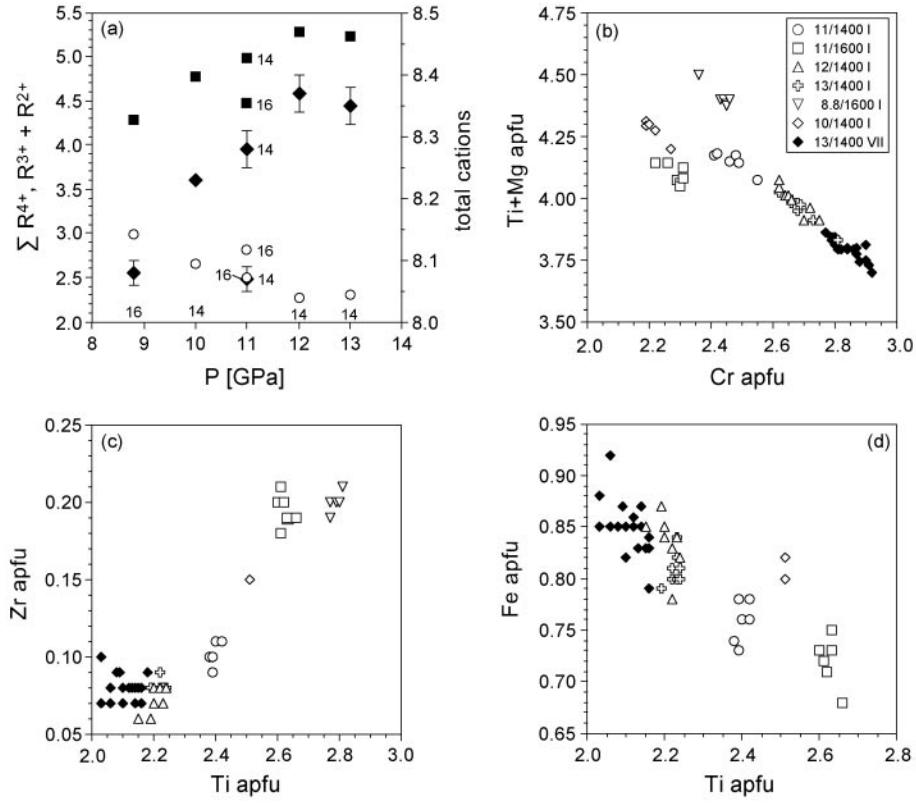

Fig. 8. (a) Variation of cation sums (a.p.f.u.) of the K–Cr-titanate (normalized to 12 oxygens) with *P* and *T*; diamonds: total cation sums (right-hand scale); squares and open circles: $\sum$Cr + Mg + Fe and $\sum$Ti + Zr, respectively (left-hand scale); (b)–(d) compositional variation (a.p.f.u.) of K–Cr-titanate in runs using bulk composition I and VII; numbers next to plot symbols [see inset in (b)] refer to *P* (GPa) and *T* (°C); Roman numbers denote bulk composition (Table 1).

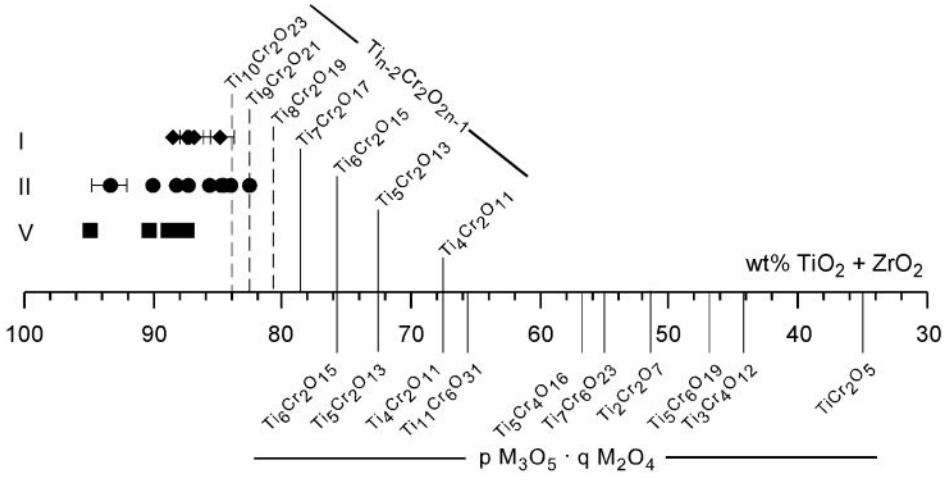

Fig. 9. Compositional variation of TiO_2 modifications in terms of Cr_2O_3–(TiO_2 + ZrO_2) for bulk compositions I (diamonds), II (circles) and V (squares); compositions of discrete Ti–Cr oxides of the $Ti_{n-2}Cr_2O_{n-1}$ and $pM_3O_5 \cdot qM_2O_4$ series are plotted for comparison.

exceed 15 mol %, thus falling into the fields of rutile *sensu stricto* and TiO_2 with crystallographic shear (Gibb & Anderson, 1972). When normalized to 1·0 cation, the maximum oxygen deficiency required to maintain charge balance is 0·09 or (Ti, Cr, Fe^{3+})$O_{1.91}$ (see Tables 3–5).

Raman spectra of rutiles were recorded from runs B01-6 and JKW43 (bulk I) at 7 and 8 GPa. All spectra show four bands at 258–261, 429–430, 614 and 693 cm^{-1} (Fig. 6c). By comparison, a spectrum of pure synthetic rutile only shows three strong bands at 240, 446 and

610 cm^{-1}. The shift of band positions in Cr-rich rutile compared with pure rutile and the appearance of the additional band at 693 cm^{-1} is thought to be due to the presence of Cr in the TiO_2 lattice. It should be noted, however, that the 693 cm^{-1} band does not correspond to any of the Cr–O vibrational modes known from Cr_2O_3 (see Brown *et al.*, 1968; Mougin *et al.*, 2001). A band shift as a result of a change in interatomic distances resulting from the high pressure of formation seems unlikely because the shift of the 446 cm^{-1} band (e.g. Ti–O stretching) towards lower wavenumbers is opposite to the shift of this band as observed in *in situ* high-pressure Raman studies (Mammone & Sharma, 1979; Liu & Mernagh, 1992). Raman spectra of TiO_2-II containing between 5 and 10 wt % Cr_2O_3 were recorded for runs JKW88 (bulk II) and JKW76 (bulk I). Eight bands were identified at 178, 285, 315, 337, 354, 426, 531 and 585 cm^{-1} (Fig. 6c). In contrast to rutile, the band positions of TiO_2-II seem to be virtually unaffected by the presence of substantial Cr and Zr, and agree very well with the positions reported by El Goresy *et al.* (2001) at 175, 285, 315, 340, 358, 428, 532 and 575 cm^{-1} for natural TiO_2-II from the Ries crater in Germany.

ZrO_2–TiO_2 solid solution

Most runs (Table 2) contain grains of a ZrO_2–TiO_2 solid solution, which, however, are usually too small to be analysed. In cases where the size permitted a reliable analysis, compositions with 30–35 wt % TiO_2 and 65–68 ZrO_2 were obtained (Tables 3–5). Normalized to two oxygens, this would be equivalent to $Ti_{0{\cdot}40–0{\cdot}44}Zr_{0{\cdot}60–0{\cdot}55}O_2$. According to Feighery *et al.* (1999), however, an orthorhombic compound $ZrTiO_4$ is stable instead of tetragonal $(Zr,Ti)O_2$ in the system ZrO_2–TiO_2 between 40 and 55 mol % ZrO_2. In the present study, $ZrTiO_4$ always shows a slight Zr excess compared with the ideal 1:1 Zr/Ti ratio.

Zr phase

With 48–58 wt % TiO_2, 21–34 wt % ZrO_2 and minor amounts of Cr, Fe and Mg (Tables 3 and 4), this phase is the most Zr rich apart from the ZrO_2–TiO_2 solid solution encountered in this study, and appears in high-temperature runs at 1600°C in bulk compositions I and II. It was one of the phases selected for structure analysis. An averaged composition derived from run JKW78 was used as starting composition for a synthesis experiment at 8·8 GPa and 1600°C. Structure analysis of a single crystal extracted from JKW81 showed that the Zr phase is isostructural with fluorite. A more complete discussion of the Zr phase structure and possible implications for fluorite-type structures at high pressures and temperatures will be presented elsewhere.

Magnetoplumbite phases

Like crichtonites, all magnetoplumbite phases in this study show a deviation from the ideal $AM_{12}O_{19}$ stoichiometry in accordance with data from natural magnetoplumbites from upper-mantle settings. Yimengite and hawthorneite synthesized at 7, 10 and 15 GPa show a range in A-site and M-site occupancies of 0·93–1·28 and 11·73–12·24 a.p.f.u., respectively. Total cation sums are in the range 12·68–13·33 (Fig. 4d–f). TiO_2 and Cr_2O_3 contents of 19–33 wt % and 33–44 wt %, respectively, are closely comparable with the compositions of natural yimengites and hawthorneites (Zhou *et al.*, 1984; Haggerty *et al.*, 1989). It is interesting to note that yimengite and hawthorneite are the only carriers of large cations in all runs using bulk compositions III and IV except in run JKW43 using bulk IV. In this run, the shift in bulk composition associated with the almost complete loss of Fe from the experimental charge resulted in the stability of an additional Ba–Cr–Ti phase (Ba phase 3, Table 6). By comparison, such partitioning of the large cation into a second phase could not be observed in JKW43 using bulk composition III at identical P and T conditions.

In all runs using bulk composition VI, the 50:50 hawthorneite–yimengite solid solution represented by this bulk composition is unstable. Instead, two coexisting Ba–K phases (HAYI and YIHA in Table 2), are present together with small amounts of unidentified phases U7–U9 (see Table 2). This is unlike the situation encountered in the lindsleyite–mathiasite system (see above) and consistent with results obtained by Foley *et al.* (1994) at somewhat lower pressures using the same bulk composition. In this study, the coexisting Ba–K phases are considered to be magnetoplumbite phases following the suggestion by Foley *et al.* (1994), and were renormalized to 19 oxygens accordingly.

Cation sums of both hawthorneite-rich and yimengite-rich solid solutions ($HAYI_{ss}$ and $YIHA_{ss}$) deviate from the ideal values. This deviation is especially pronounced for $HAYI_{ss}$, which shows total cation sums of 11·46–12·65 and M-site cation sums of 10·10–11·67 as compared with the ideal values of 13·00 and 12·00 (Fig. 10). Between 5 and 13 GPa, both hawthorneite-rich and yimengite-rich solid solutions ($HAYI_{ss}$ and $YIHA_{ss}$) show a systematic decrease in K a.p.f.u. and K/(K + Ba) along with a concomitant increase in Ba (Fig. 11c, e and f). In the case of $HAYI_{ss}$, K decreases from 0·36 to 0·06 a.p.f.u. while Ba increases from 0·68 to 1·30 a.p.f.u., resulting in a decrease in K/(K + Ba) from 0·35 to 0·04. In coexisting $YIHA_{ss}$, K decreases from 1·38 to 0·48 a.p.f.u., accompanied by an increase in Ba from 0·02 to 0·58 a.p.f.u., resulting in a decrease in K/(K + Ba) from 0·99 to 0·45. Run B02-10 shows a slight reversal of this trend with increasing Ba and K a.p.f.u., especially for $HAYI_{ss}$. The significance of this reversal, however, would have to

Table 6: Averaged and representative electron microprobe analyses of phases in the systems TiO_2–Cr_2O_3–Fe_2O_3–MgO–K_2O and TiO_2–Cr_2O_3–Fe_2O_3–FeO–MgO–BaO (bulk compositions III and IV)

Experiment:	JKW43	JKW84	JK02-12	JKW43	JKW84	B02-12	JKW43	JKW84	B02-12	B02-12	JKW43	JKW84	B02-12
P (GPa):	7	10	15	7	10	15	7	10	15	15	7	10	15
T (°C):	1300	1400	1300	1300	1400	1300	1300	1400	1300	1300	1300	1400	1300
Bulk comp.:	III	III	III	IV	IV	IV	III	III	III	III	IV	IV	IV
Phase:	yimengite			hawthorneite			U6	U6	U2	U6	Ba phase 3	U7	U7
No. of analyses:	9	13	10	7	9	8	1	8	1	1	10	1	5
TiO_2	33·3(5)	27·4(1)	26·8(6)	28·2(10)	27·8(3)	19·3(3)	30·4(4)	29·2(4)	77·9	23·0	40·2(4)	39·2	33·5(9)
Cr_2O_3	44·4(8)	39·9(2)	39·9(10)	40·6(17)	32·5(4)	33·9(9)	51·7(9)	45·8(2)	16·4	52·6	31·7(5)	25·0	32·1(16)
Fe_2O_3*	9·6(3)	17·5(2)	19·5(5)	4·7(4)	15·8(2)	16·9(4)	6·7(2)	17·9(7)	4·4	19·7	2·3(1)	20·3	22·5(7)
MgO	7·6(9)	10·3(1)	8·6(1)	12·4(4)	10·4(2)	13·3(4)	11·2(3)	8·2(2)	0·7	5·8	13·7(2)	16·3	12·1(4)
BaO	b.d.	b.d.	b.d.	15·4(1)	15·6(1)	16·8(7)	b.d.	b.d.	b.d.	b.d.	11·0(2)	b.d.	b.d.
K_2O	5·5(1)	6·8(1)	6·3(3)	b.d.	b.d.	b.d.	b.d.	b.d.	0·3	b.d.	b.d.	b.d.	b.d.
∑	100·0(10)	101·8(1)	101·1 (3)	101·2(2)	101·8(4)	100·1(7)	99·9(8)	101·0(3)	99·7	101·2	98·9(2)	100·8	100·8(6)
Oxygens	19	19	19	19	19	19							
Ti	3·69(5)	3·07(2)	3·03(7)	3·35(11)	3·31(2)	2·40(3)							
Cr	5·17(8)	4·68(2)	4·74(13)	5·07(23)	4·08(6)	4·44(1)							
Fe^{3+}	0·84(10)	1·95(2)	2·21(8)	0·55(5)	1·89(2)	2·11(6)							
Mg	2·10(7)	2·28(2)	1·92(2)	2·92(9)	2·46(4)	3·29(11)							
Ba	—	—	—	0·95(1)	0·97(1)	1·09(5)							
K	1·04(3)	1·28(1)	1·21(5)	—	—	—							
∑	12·82(5)	13·25(1)	13·10(4)	12·84(1)	12·71(1)	13·33(5)							
∑A-cations	1·04(3)	1·28(1)	1·21(5)	0·95(1)	0·97(1)	1·09(5)							
∑M-cations	11·79(5)	11·98(1)	11·90(4)	11·89(2)	11·74(1)	12·24(4)							

*Total Fe expressed as Fe_2O_3.
Numbers in parentheses represent standard deviation. Abbreviations are as in Table 2.

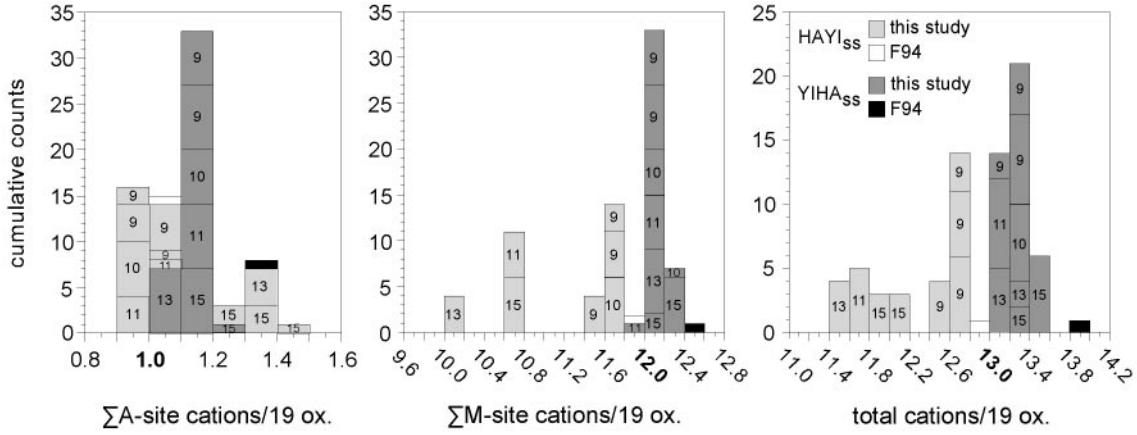

Fig. 10. Distribution of cation sums for K–Ba phases ($HAYI_{ss}$ and $YIHA_{ss}$) encountered in experiments using bulk composition VI and normalized to 19 oxygens and $Fe_{tot} = Fe^{3+}$ assuming a magnetoplumbite stoichiometry; ideal values for ∑A-site cations, ∑M-site cations and total cations are marked in bold; data from Foley *et al.* (1994) (F94) are plotted for comparison; numbers in histograms refer to experimental pressures.

be tested by additional runs. It might also be an analytical artefact as a result of the small grain size of $HAYI_{ss}$ in this run and the possibility of beam overlap with adjacent K-rich $YIHA_{ss}$ grains and/or analysis of undetected K-rich inclusions in $HAYI_{ss}$. Consistent with the results by Foley *et al.* (1994), $HAYI_{ss}$ always has lower Mg and $Mg/(Mg + Fe^{3+})$ compared with $YIHA_{ss}$ (Fig. 11b).

An interesting feature of the compositional variation of the Ba–K phases in bulk composition VI is the strong increase in the Ti/Cr ratio of $HAYI_{ss}$ above 10 GPa with an increase in Ti from 2·98 Ti a.p.f.u. at 10 GPa to 4·89 and 5·58 Ti a.p.f.u. at 11 and 13 GPa (Fig. 11a and b). A possible explanation would be Fe loss despite the use of a graphite liner because the abrupt increase in Ti/Cr of $HAYI_{ss}$ is accompanied by a strong decrease in Fe^{3+} a.p.f.u. from 1·8–1·9 at $P \leq 10$ GPa to 0·7–0·9 at 11 and 13 GPa. On the other hand, run B02-10 also produced $HAYI_{ss}$ with high Ti/Cr compared with runs at $P \leq 10$ GPa, but in this case combined with Fe^{3+} a.p.f.u. values almost identical to those encountered at low pressures. At present, the significance of this change in Ti/Cr cannot be explained satisfactorily and would require structure analysis of $HAYI_{ss}$.

Raman spectra of magnetoplumbite phases are presented in Fig. 6b. Like crichtonite phases, both yimengite and hawthorneite show relatively simple spectra with broad bands in the wavenumber region $<800\,cm^{-1}$. The most prominent feature of the yimengite spectrum is a broad double band at 629 and $695\,cm^{-1}$ with additional small bands at 545, 471 and $285\,cm^{-1}$. By comparison, only one strong band at $680\,cm^{-1}$ is present in the hawthorneite spectrum, with an additional strong band at $516\,cm^{-1}$ and small bands at 459, 352 and $285\,cm^{-1}$. The spectrum of the Ba-rich phase (HAYI) in the system yimengite–hawthorneite is similar to that of hawthorneite, with the strongest band at $678\,cm^{-1}$. The spectrum of the K-rich phase (YIHA), on the other hand, is different from either the yimengite or hawthorneite spectrum but very similar to that of the K–Cr-titanate encountered in bulk composition I. In view of the overall compositional similarity between YIHA and the K–Cr-titanate, the similarity in Raman spectra of the two phases raises the question of whether YIHA and HAYI do represent magnetoplumbite-structured phases coexisting along a solvus as suggested by Foley *et al.* (1994). An answer to this question, however, will have to await structure analysis of both YIHA and HAYI.

Unidentified phases

A number of unidentified Ti–Cr–(Ba) phases are present together with crichtonite and magnetoplumbite phases for which no data on their structures are available and a distinction is solely based on electron microprobe analysis. As noted above, the distinction is therefore somewhat arbitrary and only preliminary in the absence of data on the crystal structure of these phases. Nevertheless, a formula calculation was attempted for some of the phases to give at least an educated guess on possible stoichiometries. No attempt has been made to calculate stoichiometries based on a fixed number of cations, especially when phases contain significant Fe with an unknown Fe^{2+}/Fe^{3+} ratio, because this would place tight and unjustified constraints on cation ratios and result in grossly misleading stoichiometries.

Unidentified Ba-bearing phases (Ba phases 1–3). Two Ba-bearing Cr–Ti-rich phases appear as breakdown products of lindsleyite at pressures between 11 and 13 GPa. Both phases contain 50–52 wt % TiO_2 and 15–20 wt % Cr_2O_3 and both are significantly richer in Ba than lindsleyite, with 20·6–22·2 wt % and 15·3–17·5 wt % BaO in the Ba-rich and Ba-poor phase, respectively (Table 4).

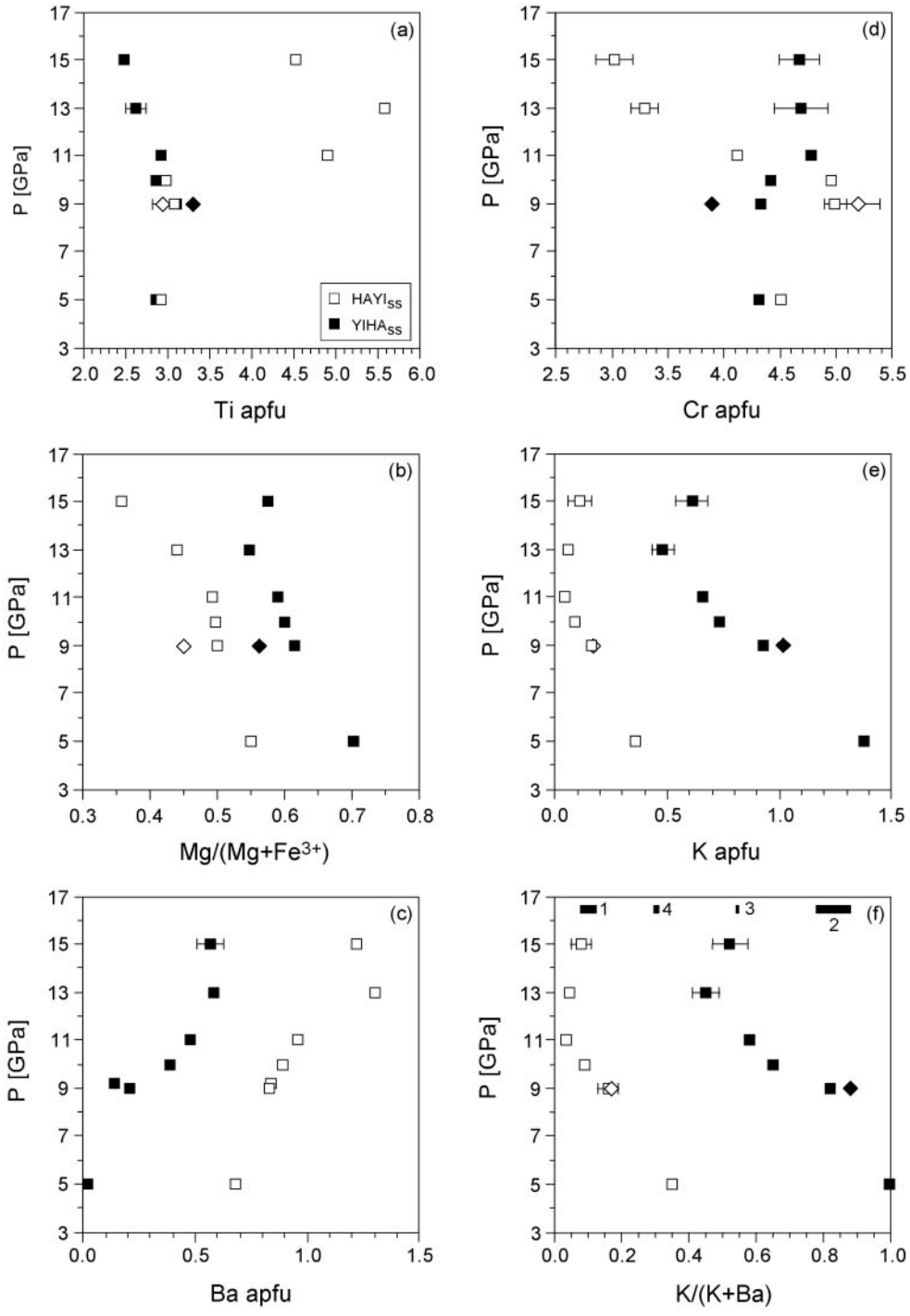

Fig. 11. (a)–(f) Variation of Ti (a.p.f.u.), Mg/(Mg + Fe^{3+}), Ba, Cr, K, and K/(K + Ba) in coexisting Ba–K phases ($HAYI_{ss}$ and $YIHA_{ss}$) encountered in experiments using bulk composition VI as a function of pressure (*P*); diamonds represent data from run B01-9; in (f), black bars denote compositional range of: (1) natural hawthorneite (Haggerty *et al.*, 1989); (2) yimengite (Nixon & Condliffe, 1989; Bulanova *et al.*, 2004); (3) Sr-magnetoplumbite (Sobolev *et al.*, 1997); (4) haggertyite (Velde, 2000).

Both Ba-bearing phases show a systematic difference in composition, with the Ba-rich phase always being richer in Ba and Ti and poorer in Zr, Cr, Fe and Mg compared with the Ba-poor phase (Table 4). Whether these two phases have similar structures and represent compositions on opposite limbs of a solvus is not known at present and would require more experiments to higher pressures to outline the shape of a potential solvus. Assuming that

both phases contain one structural position that is exclusively occupied by Ba, and that this position can be fully occupied (i.e. vacancies on the Ba position are not an integral part of the structures), then the compositions of the Ba-rich and Ba-poor phase would be consistent with BaM_8O_{15} and a $BaM_{11}O_{20}$ stoichiometry, respectively.

Ba phase 3 was found only in run JKW43 using bulk composition IV. Its appearance is thought to be due to Fe loss from bulk composition IV as a result of the lack of a graphite liner. Assuming Cr a.p.f.u. $= n \times 2$ and a separate lattice position for Ba that shows a degree of occupation similar to that of magnetoplumbites and crichtonites, then the smallest reasonable oxygen basis would be 20, resulting in a formula $Ba_{0{\cdot}88}Mg_{2{\cdot}68}(Cr,Fe^{3+})_{4{\cdot}38}Ti_{4{\cdot}94}O_{20}$ with $\sum$cations $=$ 12·00. Normalization to 19 oxygens (i.e. assuming a solvus generated by unmixing on the M-site) would result in a total cation sum and $\sum$M-site cations much lower than found in any high-pressure magnetoplumbite reported or synthesized in this study.

Unidentified Ti–Cr–Fe–Mg phases. A number of Ti–Cr–Fe–Mg phases appear in addition to the crichtonite and magnetoplumbite phases described above. Modal amounts of these phases range from ~20% to only one grain found in an individual run. These phases, labelled U1–U9 in Table 2, have a wide range in TiO_2 and Cr_2O_3 contents from 6 to 75 wt % TiO_2 and from 15 to 60 wt % Cr_2O_3. Averaged or representative compositions are listed in Tables 4–7. Some of the phases have compositions similar to natural Ti–Cr phases such as U4 and U8, or similar to phases known from low-pressure experiments such as U2.

Phase U4 is comparable in composition with a Cr–Ti oxide described by Stachel *et al.* (1998) as an inclusion in diamond that was tentatively identified as an unusually Cr-rich ilmenite. Both compositions of U4 and that reported by Stachel *et al.* (1998) are listed in Table 5. It should be noted that a wide range in Ti–Cr–Fe–Mg oxide compositions (e.g. phases U6 and U7) can be normalized to two cations and three oxygens assuming a ilmenite stoichiometry and a variation in composition as a result of an exchange $2\,(Cr + Fe^{3+}) \Leftrightarrow Ti + (Mg + Fe^{2+})$. In the absence of information on Cr_2O_3 and Fe_2O_3 solubility limits in ilmenite at high P and T, and in view of the complexity of the Cr–Ti–Fe–Mg system even at low pressures, no attempt has been made to normalize other Ti–Cr–Fe–Mg phases to an ilmenite stoichiometry.

Phase U9 was found together with U8 in run B01-7 as euhedral to subhedral crystals. It contains ~6·5 wt % TiO_2 and 60 wt % Cr_2O_3, which would be similar in composition to a Ti-rich Cr-spinel. Normalization to four oxygens and three cations yields stoichiometric coefficients that can be expressed in terms of known spinel end-members Mg_2TiO_4 (16 mol %), $FeFe_2O_4$ (5 mol %), $FeCr_2O_4$ (37 mol %) and $MgCr_2O_4$ (41 mol %) with a negligible excess of Cr_2O_3 of 0·3 mol %.

Phase U2 may be a member of the $Ti_{2-n}Cr_2O_{2n-1}$ series of Andersson phases (Flörke & Lee, 1970). Combined $TiO_2 + ZrO_2$ contents near 78 wt % indicate a compound $Ti_7Cr_2O_{17}$ ideally containing 78·6 wt % TiO_2 and 21·4 wt % Cr_2O_3. In fact, normalization of phase U2 to 17 oxygens yields $\sum$total cations = 9·04–9·18, $\sum$Ti + Zr = 6·93–7·09 and $\sum$Cr + Fe + Mg ($Fe_{tot} = Fe_2O_3$) = 1·85–2·22.

DISCUSSION

What factors govern the stability of crichtonite and magnetoplumbite phases in the upper mantle?

The formation of crichtonite and magnetoplumbite series phases is commonly attributed to metasomatic alteration of Cr-spinel in depleted Cr-rich harzburgites by incompatible (trace) element enriched fluids or melts (e.g. Nixon & Condliffe, 1989). An inclusion of Cr-rich and Al-depleted spinel coexisting with Cr-rich pyrope and enstatite in a Sr-magnetoplumbite-containing diamond described by Sobolev *et al.* (1997) also indicates a harzburgitic source for magnetoplumbite. The fact that many crichtonites and magnetoplumbites seem to have grown on pre-existing Cr-spinel (e.g. Haggerty, 1983, 1987; Nixon & Condliffe, 1989; Velde, 2000; Bulanova *et al.*, 2004) is presumably related to the similarity of spinel- and crichtonite–magnetoplumbite structures that favours nucleation of crichtonite or magnetoplumbite on a spinel substrate. The source of the Ti required for titanate formation is more equivocal. Menzies *et al.* (1987) assumed that Ti is not introduced by metasomatism but derived locally from the pre-metasomatic whole-rock Ti budget. This can be a reasonable assumption for a primitive mantle containing ~0·2 wt % TiO_2 (McDonough & Sun, 1995), but not for an average cratonic peridotite, for which McDonough (1994) and Rudnick *et al.* (1998) reported only 0·08 wt % TiO_2. The presence in crichtonite and/or magnetoplumbite assemblages of very Ti-rich Cr-spinels with up to 7 wt % TiO_2 (Nixon & Condliffe, 1989; see also Haggerty, 1983; Bulanova *et al.*, 2004) is atypical of cratonic (harzburgitic) spinels (see McDonough & Rudnick, 1998) and also suggests metasomatic addition of Ti prior to or contemporaneous with the incompatible trace element infiltration.

The presence of lindsleyite–mathiasite in spinel-free fertile metasomatized lherzolites (Konzett *et al.*, 2000; Grégoire *et al.*, 2002) shows that the presence of Cr-spinel is not an indispensible prerequisite for crichtonite phase formation in the upper mantle. Instead, silicate sources such as clinopyroxene must be invoked as the Cr source. The unusually low Cr_2O_3 contents of 7·9–10·9 wt %

Table 7: Averaged and representative electron microprobe analyses of phases in the system TiO_2–ZrO_2–Cr_2O_3–Fe_2O_3–MgO–K_2O–BaO (bulk composition VI)

Experiment:	ACT-5[1]		B02-9		B01-7		JKW84		B01-8		B01-10		B02-12	
P (GPa):	5		9		9		10		11		13		15	
T (°C):	1350		1150[2]		1300		1400		1300		1300		1300	
Phase:	HAYI	YIHA	HAYI	YIHA	HAYI	YIHA	HAYI	YIHA	HAYI	YIHA	HAYI	YIHA	HAYI	YIHA
No. of analyses:	1	1	7	6	5	7	6	6	5	7	4	8	9	8
TiO_2	24·3	25·2	24·3(10)	29·3(5)	25·6(6)	27·4(6)	24·7(1)	25·0(1)	40·7(3)	25·2(2)	45·1(3)	22·3(11)	36·8(10)	21·1(9)
Cr_2O_3	35·7	36·3	40·9(15)	32·8(5)	39·6(8)	36·4(5)	39·1(2)	36·7(1)	32·7(3)	39·0(5)	25·2(9)	37·8(18)	23·4(12)	37·7(14)
Fe_2O_3*	17·0	14·1	15·9(4)	18·9(2)	14·9(2)	16·2(1)	15·6(1)	17·2(1)	7·1(3)	14·9(3)	5·6(6)	18·5(7)	16·4(8)	18·3(7)
MgO	10·4	16·8	6·5(1)	12·2(2)	7·6(2)	13·0(2)	7·7(1)	12·9(2)	3·3(1)	11·3(2)	2·2(3)	11·3(3)	4·6(2)	12·5(3)
BaO	10·8	0·3	13·3(2)	2·4(2)	13·3(4)	3·5(2)	14·2(1)	6·6(1)	15·3(2)	7·9(2)	20·1(5)	9·5(6)	19·0(4)	9·3(9)
K_2O	1·8	7·2	0·8(1)	5·3(2)	0·8(1)	4·8(1)	0·4(0)	3·8(0)	0·2(1)	3·3(1)	0·3(1)	2·4(2)	0·5(2)	3·0(4)
$\sum$	100·0	100·0	101·6(6)	100·9(10)	101·8(3)	101·4(5)	101·7(3)	102·1(3)	99·3(2)	101·5(5)	98·5(5)	101·7(3)	100·7(5)	101·8(4)
Oxygens	19	19	19	19	19	19	19	19	19	19	19	19	19	19
Ti	2·92	2·85	2·93(12)	3·30(4)	3·07(6)	3·09(5)	2·98(1)	2·86(1)	4·89(3)	2·92(2)	5·58(1)	2·62(12)	4·52(9)	2·48(10)
Cr	4·50	4·31	5·20(19)	3·89(4)	4·99(10)	4·33(7)	4·95(2)	4·42(1)	4·12(4)	4·77(5)	3·29(12)	4·68(24)	3·02(17)	4·67(18)
Fe^{3+}	2·04	1·59	1·91(3)	2·13(2)	1·79(2)	1·83(2)	1·88(1)	1·97(2)	0·85(4)	1·73(4)	0·69(8)	2·18(7)	2·02(8)	2·16(8)
Mg	2·48	3·76	1·56(3)	2·72(3)	1·79(3)	2·92(3)	1·85(2)	2·94(4)	0·79(2)	2·49(4)	0·54(7)	2·64(6)	1·12(5)	2·92(7)
Ba	0·68	0·02	0·84(2)	0·14(1)	0·83(3)	0·21(1)	0·89(1)	0·39(1)	0·96(1)	0·48(2)	1·30(3)	0·58(4)	1·22(3)	0·57(6)
K	0·36	1·38	0·17(3)	1·02(2)	0·16(3)	0·93(2)	0·09(0)	0·73(1)	0·04(1)	0·66(1)	0·06(2)	0·48(5)	0·11(5)	0·61(7)
$\sum$	12·99	13·90	12·60(3)	13·20(1)	12·62(1)	13·30(1)	12·65(1)	13·31(1)	11·64(2)	13·15(2)	11·46(2)	13·18(3)	12·01(6)	13·41(4)
$\sum$A-cations	1·04	1·40	1·01(3)	1·16(1)	0·99(1)	1·13(1)	0·98(1)	1·12(1)	0·99(1)	1·13(1)	1·36(2)	1·06(1)	1·32(6)	1·18(3)
$\sum$M-cations	11·95	12·50	11·59(3)	12·04(2)	11·64(0)	12·16(1)	11·67(1)	12·19(2)	10·65(2)	12·02(2)	10·10(3)	12·12(3)	10·69(1)	12·23(4)
K/(K + Ba)	0·35	0·99	0·17(2)	0·88(1)	0·16(3)	0·82(1)	0·09(0)	0·65(0)	0·04(1)	0·58(1)	0·04(1)	0·45(4)	0·08(3)	0·51(5)

Experiment:	B01-9	B01-7	JKW84	B01-8	B01-10	B02-10	B01-7	B02-10	JKW86
P (GPa):	9	9	10	11	13	15	9	15	13
T (°C):	1150*	1300	1400	1300	1300	1300	1300	1300	1400
Bulk comp.:	VI	VI	VI	VI	VI	VI	VI	VI	VII
Phase:	U7	U7	U7	U7	U7	U7	U8	U9	K-tit
No. of analyses:	1	3	5	4	3	3	3	1	18
TiO_2	39·8	35·5(1)	33·2(2)	31·1(8)	32·5(2)	34·8(16)	6·4(1)	16·8	30·1(7)
ZrO_2	—	—	—	—	—	—	—	—	1·8(2)
Cr_2O_3	26·2	34·8(2)	36·5(2)	45·5(9)	33·7(6)	29·2(12)	59·9(4)	58·7	38·6(6)
Fe_2O_3*	22·0	20·0(1)	20·0(1)	15·2(5)	29·5(7)	26·1(11)	20·9(1)	18·8	12·0(6)
MgO	12·6	12·0(1)	11·4(2)	9·7(1)	17·0(3)	11·9(8)	15·2(0)	6·0	12·1(2)
BaO	b.d.	b.d.	b.d.	b.d.	b.d.	b.d.	b.d.	b.d.	—
K_2O	b.d.	b.d.	b.d.	b.d.	b.d.	b.d.	b.d.	b.d.	6·9(1)
$\sum$	102·9	102·5(3)	101·1(2)	101·8(3)	102·1(5)	102·3(5)	102·8(3)	100·3	101·5(4)
Oxygens									12
Ti									2·11(5)
Zr									0·08(1)
Cr									2·84(5)
Fe^{3+}									0·84(4)
Mg									1·68(3)
Ba									—
K									0·82(1)
$\sum$									8·38(3)

[1]Data from Foley *et al*. (1994).
[2]See Table 2 for explanation.
*Total Fe expressed as Fe_2O_3.
Numbers in parentheses represent standard deviation. Abbreviations are as in Table 2.

reported by Konzett *et al.* (2000) for LIMA may thus reflect the absence of Cr-spinel.

Apart from the availability of LILE and a local source of Cr, other factors that govern the formation of crichtonite and magnetoplumbite phases in peridotitic upper mantle remain unclear. This is especially true for magnetoplumbites because only very few occurrences are reported that represent either isolated diamond inclusions or macrocrysts from kimberite concentrates and, hence, do not allow the study of the original environment of formation. In the case of crichtonite phases, the situation is better because crichtonites are (amongst other occurrences, see above) known from a suite of metasomatized peridotites that can be placed in a genetic context (see Erlank *et al.*, 1987).

The apparent rarity of crichtonite phases as compared with the widespread presence of phlogopite and/or amphibole in metasomatized peridotites indicates that in most cases hydrous silicates preferentially incorporate LILE introduced by metasomatism. This is possible because incompatible (trace) element metasomatism is almost always accompanied by the introduction of water (e.g. Menzies & Hawkesworth, 1987, and references therein), whereby a hydrous fluid may act as a complexing agent for trace element transport. The distribution of crichtonite phases in metasomatized peridotites from the Kaapvaal Craton (Erlank *et al.*, 1987, and references therein) indicates that it is the hydrogen/LILE ratio that is critical for crichtonite stability. It is only in the most advanced states of metasomatism that LIMA phases become stable *in addition to* phlogopite and/or amphibole. To the authors' best knowledge, no occurrence of LIMA has been described where these phases are present in the absence of hydrous silicates. Therefore, it is only in cases where the ability of hydrous phases (whose modal amount is controlled by the amount of hydrogen available) to accommodate LILE is exhausted because of a high LILE/H ratio that crichtonite may become stable, provided sufficient Cr and Ti is available.

The availability of Ti is controlled by the ability of coexisting phases to incorporate this element. By far the most common metasomatic Ti phases are rutile and ilmenite, both of which may also accommodate Cr on a wt % level (e.g. Tollo & Haggerty, 1987) and are stable instead of crichtonite–magnetoplumbite if LILE are locked up in coexisting hydrous silicates. At high pressures, the ability of silicate phases to compete for Ti has to be taken into account, especially in fertile alkali-enriched bulk compositions. Peridotites sampled by kimberlites often contain garnets with high TiO_2 contents reaching wt % levels in addition to significant Na (e.g. Peltonen *et al.*, 1998; Sobolev *et al.*, 1998; Stachel *et al.*, 1998). The ability of garnet to incorporate large amounts of Ti and Na through exchange of the type $M^{+} + Ti^{4+} \Leftrightarrow M^{2+} + M^{3+}$ is confirmed by high-pressure experiments (e.g. Konzett, 1997; Zhang *et al.*, 2003). This means that in garnet-bearing systems, the availability of Ti for titanate formation decreases with increasing pressure as a result of partitioning into garnet.

A comparison of the evolution of the A-site cation occupancies in crichtonites and magnetoplumbites synthesized in the present study shows a different behaviour for the two series of phases. Crichtonites show a systematic increase in K/Ba with pressure whereas magnetoplumbites show decreasing K/Ba on both limbs of the solvus (if one accepts the idea of a solvus based on experimental evidence and in the absence of exsolution textures known from natural samples) (Figs 5 and 11). In this respect, the K–Ba systematics in crichtonites are similar to the K–Na systematics in K–Na-bearing silicates from peridotites such as amphiboles, micas (e.g. Konzett *et al.*, 1997; Konzett & Fei, 2000) and clinopyroxene (the last only at pressures >5 GPa; see Harlow, 1997). This increasing preference of silicates for K with increasing pressure is attributed to the much higher compressibility of the potassium ion and its ability to fit more tightly in the large and highly coordinated lattice positions into which both K and Na enter (e.g. Konzett *et al.*, 1997). Because no data are available on the variation in K–Ba systematics of silicates with pressure, it is not clear whether decreasing K/Ba in magnetoplumbite represents an exception to a more general preference of K over Na and other cations with large ionic radii.

Results obtained from bulk composition VI indicate that the system yimengite–hawthorneite is much more complex than the system mathiasite–lindsleyite. The compositional evolution of coexisting Ba–K phases with significant changes between 10 and 11 GPa and the similarity of Raman spectra of YIHA and the K–Cr-titanate at least hint at the possibility that phase compositions and structures in the system yimengite–hawthorneite are not simply controlled by a solvus. Further investigations will, however, be required to gain a more comprehensive understanding of this system.

The potential role of oxide phases as LILE carriers

Amongst the multitude of natural LILE-bearing titanates primarily known from kimberlites and lamproites (see Haggerty, 1987; Mitchell & Bergman, 1991; Mitchell, 1995) only members of the crichtonite and magnetoplumbite series of phases in addition to priderite are known to occur as presumably syngenetic inclusions in diamonds (Sobolev *et al.*, 1988, 1997; Jaques *et al.*, 1989; Kopylova *et al.*, 1997; Bulanova *et al.*, 2004). Synthesis experiments by Foley *et al.* (1994) at 5 GPa and 1350°C confirmed the high-pressure stability of these phases. The presence in a diamond of a Cr–Sr-rich loparite containing 4·4 wt % K_2O reported by Kopylova *et al.* (1997) from

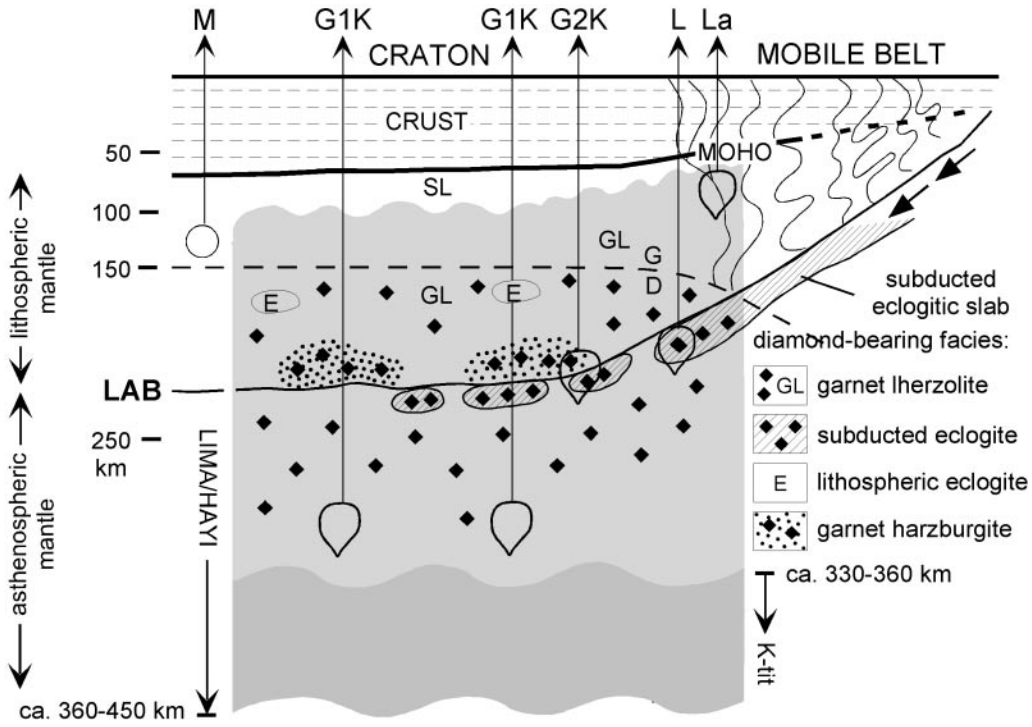

Fig. 12. Hypothetical cross-section of a craton and adjacent mobile belt modified after Mitchell (1991), showing possible source regions of melilitites (M), lamproites (L), alkaline lamprophyres (La), group 1 kimberlites (G1K) and group II kimberlites (orangeites) (G2K) in the lithosphere and asthenosphere in the stability fields of diamond (D) or graphite (G) and with various sources of xenocrystal diamonds [for further details see Mitchell (1991)]; by comparison, the approximate stability fields of alkali-titanates of the LIMA and HAYI series and of selected breakdown products are shown by shaded areas; their upper and lower *P* stability limits are based on experiments of this study [see also Foley *et al.* (1994)] and on geothermobarometry of natural titanate-bearing rocks (Waters & Erlank, 1988; Wang *et al.*, 1999), respectively. SL, spinel lherzolite; LAB, lithosphere–asthenosphere boundary.

the River Ranch kimberlite, Limpopo belt, SE Africa, however, was attributed by those workers to growth of this phase outside the stability field of diamond.

Experiments in this study indicate that Ba- and K-rich members of the crichtonite and magnetoplumbite series of phases have P–T stability fields that extend far into the diamond stability field to a depth of at least 300 km in the case of crichtonites and to at least 400–450 km in the case of magnetoplumbites. Breakdown of crichtonite phases between 11 and 12 GPa leads to the formation of new K- and Ba-titanates that may act as LILE carriers to even greater depths. The temperatures at which magnetoplumbite and crichtonite phases were synthesized in the present study are as high as 1400–1600°C, which suggests that these phases would be stable not only throughout the entire continental (cratonic) lithosphere but also along an average present-day mantle adiabat in the underlying asthenosphere (Fig. 12). P–T estimates of 6–7 GPa at 1300–1500°C reported by Leost *et al.* (2003) for a diamond inclusion suite including a Cr-titanate (crichtonite according to those workers) + Ti-rich phlogopite would thus be consistent with the results of this study. Once crichtonite and/or magnetoplumbite phases have formed by metasomatic alteration of a sufficiently Cr- and Ti-rich source, they may act as an important source of LILE and HFSE during partial melting of the lithosphere or asthenosphere even if present only in trace amounts. K–Ba-titanates of the crichtonite and magnetoplumbite series of phases can thus be expected in the source regions of lamproites and both group I and group II (orangeites *sensu* Mitchell, 1995) kimberlites (see Foley, 1992*a*; Mitchell, 1995) (Fig. 12), although one should not take this to imply that these phases are commonly present.

Most recently, Bulanova *et al.* (2004) reported 124 ppm Rb, 3·7 ppm Cs and 2543 ppm Sr in syngenetic yimengite inclusions in diamond, underlining the importance of this phase as an LILE carrier. Likewise, extremely high LILE and HFSE concentrations reaching wt % levels for SrO, BaO and ZrO_2 and >1000 ppm for REE are known from LIMA phases (Jones & Ekambaram, 1982; Grégoire *et al.*, 2002). Unfortunately, no data are available on the near-solidus behaviour of crichtonites and magnetoplumbites in a metasomatized peridotite. Therefore, it is not known (1) whether these phases can coexist with a partial melt and control its LILE budget and (2) whether they would survive thermal erosion of the lithosphere and become entrained in convecting asthenospheric mantle.

The role of pseudobrookite (armalcolite) [(Mg,Fe)Ti_2O_5] as an LILE carrier in the upper mantle remains unclear. The pseudobrookite structure does not possess large interstitial cation sites suitable for LILE (see Yang & Hazen, 1998, and references therein). On the other hand, up to 0·30 wt % K_2O and 0·77 wt % BaO have been reported for Cr-rich armalcolites by Haggerty (1983). Jaques *et al.* (1990) gave even higher K_2O concentrations of up to 2·10 wt % for armalcolites from diamond-bearing peridotites sampled by the Argyle lamproite. Experiments by Friel *et al.* (1977) have shown that pseudobrookite $(Mg_{0·5}Fe_{0·5})Ti_2O_5$ breaks down at $P \geq 1·5$ GPa and 1200°C to form rutile + ilmenite. Hence, pseudobrookite would act as an LILE carrier in shallow upper mantle only. This is consistent with an occurrence of armalcolite coexisting with feldspar reported by Grégoire *et al.* (2000*b*) for which *P–T* conditions of 1·3 GPa and 1150–1200°C have been estimated.

SUMMARY OF CONCLUSIONS

(1) High-*P–T* experiments have been conducted in the range 7–15 GPa and 1150–1600°C to determine the *P–T* stability and breakdown products of K- and Ba-dominant members of the crichtonite ($AM_{21}O_{38}$) and magnetoplumbite ($AM_{12}O_{19}$) series of phases.

(2) Lindsleyite (LIN) $Ba(Ti_{12}Cr_4Fe_2ZrMg_2)O_{38}$ and mathiasite (MA) $K(Ti_{13}Cr_4FeZrMg_2)O_{38}$ are stable to 11 GPa and 1500–1600°C. Between 11 and 12 GPa, lindsleyite breaks down to form two Ba–Cr-titanates of unknown structure that persist to at least 13 GPa. The high-*P* breakdown product of mathiasite is a K–Cr-titanate with an idealized formula KM_7O_{12}, where M = Ti, Cr, Mg, Fe. This phase possesses space group $P6_3/m$ with $a = 9·175(2)$ Å, $c = 2·879(1)$ Å, $V = 209·9(1)$ Å^3.

(3) Hawthorneite (HA) $Ba(Ti_3Cr_4Fe_2Mg_3)O_{19}$ and yimengite (YI) $K(Ti_3Cr_5Fe_2Mg_2)O_{19}$, are stable in runs at 7, 10 and 15 GPa between 1300 and 1400°C coexisting with a number of Ti–Cr-oxides.

(4) Molar mixtures (1:1) of LIMA and HAYI were studied at 7–10 GPa and 1300–1400°C, and 9–15 GPa and 1150–1400°C, respectively. In the system LIMA, one homogeneous Ba–K phase is stable, which shows a systematic increase in the K/(K + Ba) ratio with increasing *P*. In the system HAYI, two coexisting Ba–K phases appear, which are Ba rich and Ba poor, respectively. This is consistent with results obtained by Foley *et al.* (1994).

(5) Results of this study suggest that crichtonite and magnetoplumbite phases are potentially stable throughout the entire subcontinental lithosphere and the underlying asthenosphere to a depth of up to 450 km, and may thus be present in the source regions of both group I and group II kimberlites and lamproites, where these phases would act as major LILE and HFSE carriers. At still higher pressures, both K and Ba may remain stored in alkali-titanates.

(6) By comparison with natural LIMA phase assemblages, we conclude that only in the most advanced stages of upper-mantle metasomatism would LIMA phases become stable in addition to phlogopite and/or amphibole. It is only in cases where the ability of hydrous phases to accommodate LILE is exhausted as a result of a high LILE/H ratio that LIMA phases may form, provided sufficient Cr and Ti is available. The same is probably true for HAYI phases. Because of increased partitioning of Ti into garnet via coupled substitutions involving Na, the availability of Ti for oxide formation in general decreases with increasing *P*.

(7) An important aspect of the high-*P–T* stability of LIMA and HAYI phases not covered by this study is their near-solidus behaviour. In particular, it is not known whether these phases possess a supersolidus stability in peridotitic systems and, hence, can control the LILE and HFSE budget of low-percentage partial melts by solid–melt partitioning or whether they break down at the solidus without the ability to buffer the melt composition.

ACKNOWLEDGEMENTS

We gratefully acknowledge the help of Christos Haddidiacos, Geophysical Laboratory, and Theodoros Ntaflos, University of Vienna, during microprobe analysis. We are also indebted to Erwin Mayer and Christoph Salzmann, Department of Inorganic Chemistry, University of Innsbruck, for providing access to the Raman spectrometer and for assistance during recording of the spectra. Reviews by Michel Grégoire, Ben Harte and Nick Sobolev helped to improve the quality of the manuscript. Financial support for this study was provided by the Carnegie Institution of Washington and by the European High-Pressure Facility EU 'Access to Research Infrastructures' Programme during a visit of the first author to the Bavarian Research Institute of Experimental Geochemistry and Geophysics, University of Bayreuth.

REFERENCES

Adelsköld, V. (1938). X-ray studies on magnetoplumbite, $PbO·6Fe_2O_3$ and other substances resembling 'beta-alumina', $Na_2O·11Al_2O_3$. *Arkiv før Kemi Mineralogioch Geologi, Series A-12* **29**, 1–9.

Bertka, C. M. & Fei, Y. (1997). Mineralogy of the Martian interior up to core–mantle boundary pressures. *Journal of Geophysical Research* **102**, 5251–5264.

Brown, D. A., Cunningham, D. & Glass, W. K. (1968). The infrared and Raman spectra of chromium (III) oxide. *Spectrochimica Acta* **24A**, 965–968.

Bulanova, G. P., Muchemwa, E., Pearson, G., Griffin, B. J., Kelly, S., Klemme, S. & Smith, C. B. (2004). Syngenetic inclusions of

yimengite in diamond from Sese kimberlite (Zimbabwe)—evidence for metasomatic conditions of growth. *Lithos* **77**, 181–192.

Chase, A. B. & Wolten, G. M. (1965). Aluminum and gallium analogs of magnetoplumbite. *Journal of the American Ceramic Society* **48**, 276–277.

Dawson, J. B. & Smith, J. W. (1977). The MARID (mica–amphibole–rutile–ilmenite–diopside) suite of xenoliths in kimberlite. *Geochimica et Cosmochimica Acta* **41**, 309–323.

Dirstine, R. T. & Rosa, C. J. (1979). Defect structure and related thermodynamic properties of nonstoichiometric rutile (TiO_{2-x}) and Nb_2O_5 doped rutile. Part I: The defect structure of TiO_{2-x} (rutile) and partial molar properties for oxygen solution at 1273 K. *Zeitschrift für Metallkunde* **70**, 322–329.

El Goresy, A., Chen, M., Gillet, P., Dubrovinsky, L., Graup, G. & Ahuja, R. (2001). A natural shock-induced dense polymorph of rutile with α-PbO_2 structure in the suevite from the Ries crater in Germany. *Earth and Planetary Science Letters* **192**, 485–495.

Erlank, A. J., Waters, F. G., Hawkesworth, C. J., Haggerty, S. E., Rickard, R. S. & Menzies, M. (1987). Evidence for mantle metasomatism in peridotite nodules from Kimberley pipes, South Africa. In: Menzies, M. & Hawkesworth, C. J. (eds) *Mantle Metasomatism*. London: Academic Press, pp. 221–312.

Feighery, A. J., Irvine, J. T. S., Flagg, D. P. & Kaiser, A. (1999). Phase relations at 1500°C in the ternary system ZrO_2–Y_2O_3–TiO_2. *Journal of Solid State Chemistry* **143**, 273–276.

Flörke, O. W. & Lee, C. W. (1970). Andersson Phasen, dichteste Packung und Wadsley Defekte im System Ti–Cr–O. *Journal of Solid State Chemistry* **1**, 445–453.

Foley, S. F. (1992*a*). Petrological characterization of the source components of potassic magmas: geochemical and experimental constraints. *Lithos* **28**, 187–204.

Foley, S. F. (1992*b*). Vein-plus-wall-rock melting mechanisms in the lithosphere and the origin of potassic alkaline magmas. *Lithos* **28**, 435–453.

Foley, S. F., Höfer, H. & Brey, G. (1994). High-pressure synthesis of priderite and members of the lindsleyite–mathiasite and hawthorneite–yimengite series. *Contributions to Mineralogy and Petrology* **117**, 164–174.

Fraser, K. J., Hawkesworth, C. J., Erlank, A. J., Mitchell, R. H. & Scott-Smith, B. H. (1985). Sr, Nd, and Pb isotope and minor element geochemistry of lamproites and kimberlites. *Earth and Planetary Science Letters* **76**, 57–70.

Friel, J. J., Harker, R. I. & Ulmer, G. C. (1977). Armalcolite stability as a function of pressure and oxygen fugacity. *Geochimica et Cosmochimica Acta* **41**, 403–410.

Gatehouse, B. M., Grey, I. E. & Smyth, J. R. (1983). Structure refinement of mathiasite $(K_{0.62}Na_{0.14}Ba_{0.14}Sr_{0.10})\sum_{1.0}[Ti_{12.90}Cr_{3.10}Mg_{1.53}Fe_{2.15}Zr_{0.67}Ca_{0.29}(V,Nb,Al)_{0.36}]\sum_{21.0}O_{38}$. *Acta Crystallographica, Section C* **39**, 421–422.

Gibb, R. M. & Anderson, J. S. (1972). The system TiO_2–Cr_2O_3: electron microscopy of solid solutions and crystallographic shear structures. *Journal of Solid State Chemistry* **4**, 379–390.

Grégoire, M., Moine, B. N., O'Reilly, S., Cottin, J. Y. & Giret, A. (2000*a*). Trace element residence and partitioning in mantle xenoliths metasomatized by highly alkaline, silicate- and carbonate-rich melts (Kerguelen Islands, Indian Ocean). *Journal of Petrology* **41**, 477–509.

Grégoire, M., Lorand, J. P., O'Reilly, S. Y. & Cottin, J. Y. (2000*b*). Armalcolite-bearing, Ti-rich metasomatic assemblages in harzburgitic xenoliths from the Kerguelen Islands: implications for the oceanic mantle budget of high-field strength elements. *Geochimica et Cosmochimica Acta* **64**, 673–694.

Grégoire, M., Bell, D. R. & LeRoex, A. P. (2002). Trace element geochemistry of phlogopite-rich mafic mantle xenoliths; their classification and their relationship to phlogopite-bearing peridotites and kimberlites. *Contributions to Mineralogy and Petrology* **142**, 603–625.

Grey, I. E., Reid, A. F. & Allpress, J. G. (1973). Compounds in the system Cr_2O_3–Fe_2O_3–TiO_2–ZrO_2 based on intergrowth of the α-PbO_2 and V_3O_5 structural types. *Journal of Solid State Chemistry* **8**, 86–99.

Grey, I. E., Lloyd, D. J. & White, J. S. (1976). The structure of crichtonite and its relationship to senaite. *American Mineralogist* **61**, 1203–1212.

Grey, I. E., Madsen, I. C. & Haggerty, S. E. (1987). Structure of a new upper-mantle, magnetoplumbite-type phase, $Ba[Ti_3Cr_4Fe_4Mg]O_{19}$. *American Mineralogist* **72**, 633–636.

Grey, I. E., Velde, D. & Criddle, A. J. (1998). Haggertyite, a new magnetoplumbite-type mineral from the Prairie Creek (Arkansas) lamproite. *American Mineralogist* **83**, 1323–1329.

Haggerty, S. E. (1983). The mineral chemistry of new titanates from the Jagersfontein kimberlite, South Africa, implications for matasomatism in the upper mantle. *Geochimica et Cosmochimica Acta* **47**, 1833–1854.

Haggerty, S. E. (1987). Metasomatic mineral titanates in upper mantle xenoliths. In: Nixon, P. H. (ed.) *Mantle Xenoliths*. New York: John Wiley, pp. 671–690.

Haggerty, S. E. (1991). Oxide textures—a mini atlas. In: Lindsley, D. H. (ed.) *Oxide Minerals: Petrologic and Magnetic Significance. Mineralogical Society of America, Reviews in Mineralogy* **25**, 130–218.

Haggerty, S. E., Smyth, J. R., Erlank, A. J., Rickard, R. S. & Danchin, R. V. (1983). Lindsleyite (Ba) and mathiasite (K): two new chromium-titanates in the crichtonite series from the upper mantle. *American Mineralogist* **68**, 494–505.

Haggerty, S. E., Grey, I. E., Madsen, I. C., Criddle, A. J., Stanley, C. J. & Erlank, A. J. (1989). Hawthorneite, $Ba[Ti_3Cr_4Fe_4Mg]O_{19}$: a new metasomatic magnetoplumbite-type mineral from the upper mantle. *American Mineralogist* **74**, 668–675.

Harlow, G. E. (1997). K in clinopyroxene at high pressure and temperature: an experimental study. *American Mineralogist* **82**, 259–269.

Harte, B. (1987). Metasomatic events recorded in mantle xenoliths: an overview. In: Nixon, P. H. (ed.) *Mantle Xenoliths*. New York: John Wiley, pp. 625–640.

Harte, B., Winterburn, P. A. & Gurney, J. J. (1987). Metasomatic and enrichment phenomena in garnet peridotite facies mantle xenoliths from the Matsoku Kimberlite pipe, Lesotho. In: Menzies, M. A. & Hawkesworth, C. J. (eds) *Mantle Metasomatism*. London: Academic Press, pp. 145–219.

Jaques, A. L., Hall, A. E., Sheraton, J. W., Smith, C. B., Sun, S., Drew, R. M., Foudoulis, C. & Ellingsen, K. (1989). Composition of crystalline inclusions and C-isotopic composition of Argyle and Ellendale diamonds. In: Jaques, A. L., Ferguson, J. & Green, D. H. (eds) *Kimberlites and Related Rocks 2: Their Mantle/Crust Setting. Geological Society of Australia Special Publication* **14**, 966–989.

Jaques, A. L., O'Neill, H. St. C., Smith, C. B., Moon, J. & Chappell, B. W. (1990). Diamondiferous peridotite xenoliths from the Argyle (AK1) lamproite pipe, Western Australia. *Contributions to Mineralogy and Petrology* **104**, 255–276.

Jones, A. P. & Ekambaram, V. (1985). New INAA analysis of a mantle derived titanate mineral of the crichtonite series, with particular reference to the rare earth elements. *American Mineralogist* **70**, 414–418.

Jones, A. P., Smith, J. V. & Dawson, J. B. (1982). Mantle metasomatism in 14 veined peridotites from Bultfontein mine, South Africa. *Journal of Geology* **90**, 435–453.

Kempton, P. D. (1987). Mineralogical and geochemical evidence for differing styles of metasomatism in spinel lherzolite xenoliths: enriched mantle source regions of basalts? In: Menzies, M. A. &

Hawkesworth, C. J. (eds) *Mantle Metasomatism*. London: Academic Press, pp. 45–89.

Kiviets, G., Phillips, D., Shee, S. R., Vercoe, S. C., Barton, E. S., Smith, C. B. & Fourie, L. F. (1998). $^{40}Ar/^{39}Ar$ dating of yimengite from the Turkey Well kimberlite, Australia: the oldest and the rarest. In: *Extended Abstracts of the 7th International Kimberlite Conference*. Cape Town: University of Cape Town, pp. 432–433.

Kohn, J. A. & Eckart, D. W. (1965). Mixed-layer polytypes related to magnetoplumbite. *American Mineralogist* **50**, 1371–1380.

Konzett, J. (1997). Phase relations and chemistry of Ti-rich K-richterite-bearing mantle assemblages: an experimental study to 8·0 GPa in a Ti–KNCMASH system. *Contributions to Mineralogy and Petrology* **128**, 385–404.

Konzett, J. & Fei. Y. (2000). Transport and storage of potassium in the Earth's upper mantle and transition zone: an experimental study to 23 GPa in simplified and natural bulk compositions. *Journal of Petrology* **41**, 583–603.

Konzett, J. & Ulmer, P. (1999). The stability of hydrous potassic phases in lherzolitic mantle—an experimental study to 9·5 GPa in simplified and natural bulk compositions. *Journal of Petrology* **40**, 629–652.

Konzett, J. & Yang, H. (2001). Phase relations and crystal chemistry of complex titanates under upper mantle *P–T* conditions. *Journal of Conference Abstracts* **6**(1), 579.

Konzett, J., Sweeney, R. J., Thompson, A. B. & Ulmer, P. (1997). Potassium amphibole stability in the upper mantle: an experimental study in a peralkaline KNCMASH system to 8·5 GPa. *Journal of Petrology* **38**, 537–568.

Konzett, J., Armstrong, R. A. & Günther, D. (2000). Modal metasomatism in the Kaapvaal craton lithosphere: constraints on timing and genesis from U–Pb zircon dating of metasomatized peridotites and MARID-type xenoliths. *Contributions to Mineralogy and Petrology* **139**, 704–719.

Kopylova, M. G., Rickard, R. S., Kleyenstueber, A., Taylor, W. R., Gurney, J. J. & Daniels, L. R. M. (1997). First occurrence of strontian K–Cr-loparite and Cr-chevkinite in diamonds. *Russian Geology and Geophysics* **38**, 405–420.

Kostrovitsky, S. I. & Garanin, V. K. (1991). Chrome titanate inclusions of unusual composition in pyropes from lamprophyres and kimberlites. In: *Extended Abstracts of the 5th International Kimberlite Conference*, pp. 525–526.

Krauskopf, K. B. (1988). Geology of high-level nuclear waste disposal. *Annual Review of Earth and Planetary Sciences* **16**, 173–200.

Leost, I., Stachel, T., Brey, G. P., Harris, J. W. & Ryabchikov, I. D. (2003). Diamond formation and source carbonation: mineral associations in diamonds from Namibia. *Contributions to Mineralogy and Petrology* **145**, 15–24.

Linde, K. & DeCarli, P. S. (1969). Polymorphic behaviour of titania under dynamic loading. *Journal of Chemical Physics* **50**, 319–325.

Liu, L.-G. & Mernagh, T. P. (1992). Phase transitions and Raman spectra of anatase and rutile at high pressures and room temperature. *European Journal of Mineralogy* **4**, 45–52.

Mammone, J. F. & Sharma, S. K. (1979). Raman study of TiO_2 under high pressures at room temperature. *Carnegie Institution of Washington Yearbook* **78**, 636–640.

McDonough, W. F. (1994). Chemical and isotopic systematics of continental lithospheric mantle. In: Meyer, H. O. A. & Leonardos, O. H. (eds) *Proceedings of the 5th International Kimberlite Conference*. Brasilia: Companhia de Pesquisa de Recursos Minerais, pp. 478–485.

McDonough, W. F. & Rudnick, R. L. (1998). Mineralogy and composition of the upper mantle. In: Hemley, R. J. (ed.) *Ultrahigh-Pressure Mineralogy: Physics and Chemistry of the Earth's Deep Interior. Mineralogical Society of America, Reviews in Mineralogy* **37**, 139–164.

McDonough, W. F. & Sun, S.-s. (1995). The composition of the Earth. *Chemical Geology* **120**, 223–253.

Menzies, M. A. & Hawkesworth, C. J. (eds) (1987). *Mantle Metasomatism*. London: Academic Press, 472 pp.

Menzies, M. A., Rogers, N., Tindle, A. & Hawkesworth, C. J. (1987). Metasomatic and enrichment processes in lithospheric peridotites, an effect of asthenosphere–lithosphere interaction. In: Menzies, M. A. & Hawkesworth, C. J. (eds) *Mantle Metasomatism*. London: Academic Press, pp. 313–359.

Mitchell, R. H. (1977). Geochemistry of magnesian ilmenites from kimberlites in South Africa and Lesotho. *Lithos* **10**, 29–37.

Mitchell, R. H. (1991). Kimberlites and lamproites: primary sources of diamonds. *Geoscience Canada* **18**, 1–16.

Mitchell, R. H. (1995). *Kimberlites, Orangeites and Related Rocks*. New York: Plenum, 410 pp.

Mitchell, R. H. & Bergman, S. C. (1991). *The Petrology of Lamproites*. New York: Plenum, 447 pp.

Mitchell, R. H. & Lewis, R. D. (1983). Priderite-bearing xenoliths from the Prairie Creek mica peridotite, Arkansas. *Canadian Mineralogist* **21**, 59–64.

Mougin, J., Le Bihan, T. & Lucazeau, G. (2001). High-pressure study of Cr_2O_3 obtained by high-temperature oxidation by X-ray diffraction and Raman spectroscopy. *Journal of Physics and Chemistry of Solids* **62**, 553–563.

Nixon, P. H. & Condliffe, E. (1989). Yimengite of K–Ti metasomatic origin in kimberlitic rocks from Venezuela. *Mineralogical Magazine* **53**, 305–309.

Obradors, X., Collomb, A., Pernet, M., Samaras, D. & Joubert, J. C. (1985). X-ray analysis of the structural and dynamic properties of $BaFe_{12}O_{19}$, hexagonal ferrite at room temperatures. *Journal of Solid State Chemistry* **56**, 171–181.

Peltonen, P., Huhma, H., Tyni, M. & Shimizu, N. (1998). Garnet peridotite xenoliths from kimberlites of Finland: nature of the continental mantle at an Archaean Craton–Proterozoic mobile belt transition. In: Gurney, J. J., Gurney, J. L., Pascoe, M. & Richardson, S. H. (eds) *Proceedings of the 7th International Kimberlite Conference*. Cape Town: Red Roof Design, pp. 664–676.

Peterson, R. C. & Grey, I. E. (1995). Preparation and structure refinement of synthetic Ti^{3+}-containing lindsleyite, $BaMn_3Ti_{18}O_{39}$. *Canadian Mineralogist* **33**, 1083–1089.

Podpora, C. & Lindsley, D. H. (1984). Lindsleyite and mathiasite: synthesis of chromium-titanates in the crichtonite ($A_1M_{21}O_{38}$) series. *EOS Transactions, American Geophysical Union* **65**, 293.

Rouse, R. C. & Peacor, D. R. (1968). The relationship between senaite, magnetoplumbite and davidite. *American Mineralogist* **53**, 869–879.

Rubie, D. C., Karato, S., Yan, H. & O'Neill, H. St. C. (1993). Low differential stress and controlled chemical environment in multi-anvil high pressure devices. *Physics and Chemistry of Minerals* **20**, 315–322.

Rudnick, R. L., McDonough, W. F. & O'Connell, R. J. (1998). Thermal structure, thickness and composition of continental lithosphere. *Chemical Geology* **145**, 399–415.

Schulze, D. J., Anderson, P. F. N., Hearn, B. C. & Hetman-Casey, M. (1995). Origin and significance of ilmenite megacrysts and macrocrysts from kimberlite. *International Geology Review* **37**, 780–812.

Sobolev, N. V. & Yefimova, E. S. (2000). Composition and petrogenesis of Ti-oxides associated with diamonds. *International Geology Review* **42**, 758–767.

Sobolev, N. V., Yefimova, E. S., Kaminskiy, F. V., Lavrientiev, Y. G. & Usova, L. V. (1988). Titanate of complex composition and phlogopite in the diamond stability field. In: *Composition and Processes of Deep-seated Zones of Continental Lithosphere*. Novosibirsk: Nauka, pp. 185–186.

Sobolev, N. V., Kaminsky, F. V., Griffin, W. L., Yefimova, E. S., Win, T. T., Ryan, C. G. & Botkunov, A. I. (1997). Mineral inclusions in diamonds from the Sputnik kimberlite pipe, Yakutia. *Lithos* **39**, 135–157.

Sobolev, N. V., Yefimova, E. S. & Koptil, V. I. (1998). Mineral inclusions in diamonds in the northeast of the Yakutian diamondiferous province. In: Gurney, J. J., Gurney, J. L., Pascoe, M. & Richardson, S. H. (eds) *Proceedings of the 7th International Kimberlite Conference*. Cape Town: Red Roof Design, pp. 816–822.

Stachel, T., Harris, J. W. & Brey, G. P. (1998). Rare and unusual mineral inclusions in diamonds from Mwadui, Tanzania. *Contributions to Mineralogy and Petrology* **132**, 34–47.

Tainton, K. M. & McKenzie, D. (1994). The generation of kimberlites, lamproites, and their source rocks. *Journal of Petrology* **35**, 787–817.

Thompson, J. B., Jr (1978). Biopyriboles and polysomatic series. *American Mineralogist* **63**, 239–249.

Tollo, R. P. & Haggerty, S. E. (1987). Nb–Cr-rutile in the Orapa Kimberlite, Botswana. *Canadian Mineralogist* **25**, 251–264.

Townes, W. D., Fang, J. H. & Perrotta, A. J. (1967). The crystal structure and refinement of ferrimagnetic barium ferrite of $BaFe_{12}O_{19}$. *Zeitschrift für Kristallographie* **125**, 437–449.

Varlamov, D. A., Garanin, V. K. & Kostrovitskiy, S. I. (1996). Exotic high-titanium minerals as inclusions in garnets from lower crustal and mantle xenoliths. *Transactions of the Russian Academy of Science, Earth Science Section* **345A**, 352–355.

Velde, D. (2000). Mineralogy of mafic xenoliths and their reaction zones in the olivine lamproite from Prairie Creek Arkansas and the paragenesis of haggertyite, $Ba[Fe_6Ti_5Mg]O_{19}$. *American Mineralogist* **85**, 420–429.

Walker, D. (1991). Lubrication, gasketing, and precision in multianvil experiments. *American Mineralogist* **76**, 1092–1100.

Wang, L., Essene, E. J. & Zhang, Y. (1999). Mineral inclusions in pyrope crystals from Garnet Ridge, Arizona, USA: implications for processes in the upper mantle. *Contributions to Mineralogy and Petrology* **135**, 164–178.

Waters, F. G. & Erlank, A. J. (1988). Assessment of the vertical extent and distribution of mantle metasomatism below Kimberley, South Africa. *Journal of Petrology, Special Lithosphere Issue*, 185–204.

Withers, A. C., Essene, E. J. & Zhang, Y. (2003). Rutile/TiO_2-II phase equilibria. *Contributions to Mineralogy and Petrology* **145**, 199–204.

Yang, H. & Hazen, R.M. (1998). Crystal chemistry of cation order–disorder in pseudobrookite-type $MgTi_2O_5$. *Journal of Solid State Chemistry* **138**, 238–244.

Zhang, R. Y., Zhai, S. M., Fei, Y. M. & Liou, J. G. (2003). Titanium solubility in coexisting garnet and clinopyroxene at very high pressure: the significance of exsolved rutile in garnet. *Earth and Planetary Science Letters* **216**, 591–601.

Zhou, J., Yang, G. & Zhang, J. (1984). Mathiasite in kimberlite of China. *Acta Mineralogica Sinica* **9**, 193–200.